iScience

CellPress
OPEN ACCESS

Article

Mapping the cellular and molecular landscape of cardiac non-myocytes in murine diabetic cardiomyopathy

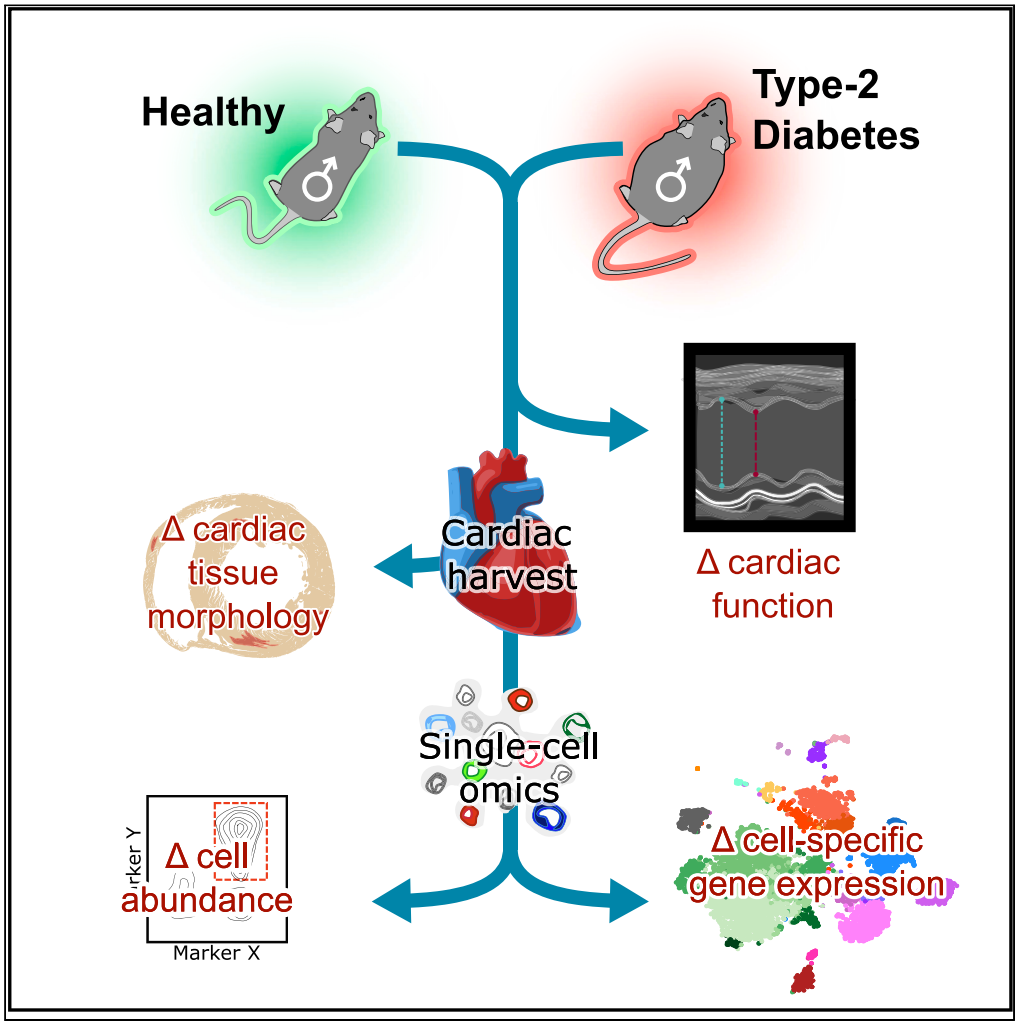

Charles D. Cohen, Miles J. De Blasio, Gabriella E. Farrugia, ..., Grant R. Drummond, Rebecca H. Ritchie, Alexander R. Pinto

rebecca.ritchie@monash.edu (R.H.R.)
alex.pinto@baker.edu.au (A.R.P.)

Highlights

Type-2 diabetes elicits cell-specific transcriptomic changes in the heart

Diabetic *(db/db)* mice show heart impairment and fibroblast expansion without fibrosis

Cytoprotective heat shock proteins are reduced in *db/db* mouse heart vascular cells

Macrophage abundance is reduced, and heterogeneity altered in *db/db* mouse hearts

Cohen et al., iScience 26, 107759
October 20, 2023
https://doi.org/10.1016/j.isci.2023.107759

iScience

CellPress
OPEN ACCESS

Article

Mapping the cellular and molecular landscape of cardiac non-myocytes in murine diabetic cardiomyopathy

Charles D. Cohen,[1,3,4,5,9] Miles J. De Blasio,[3,8,9] Gabriella E. Farrugia,[1,7] Malathi S.I. Dona,[1] Ian Hsu,[1] Darnel Prakoso,[3] Helen Kiriazis,[2,6] Crisdion Krstevski,[1,4,5] David M. Nash,[3] Mandy Li,[3] Taylah L. Gaynor,[1,4,5] Minh Deo,[3] Grant R. Drummond,[5] Rebecca H. Ritchie,[3,4,5,10,*] and Alexander R. Pinto[1,4,5,6,10,11,*]

SUMMARY

Diabetes is associated with a significantly elevated risk of heart failure. However, despite extensive efforts to characterize the phenotype of the diabetic heart, the molecular and cellular protagonists that underpin cardiac pathological remodeling in diabetes remain unclear, with a notable paucity of data regarding the impact of diabetes on non-myocytes within the heart. Here we aimed to define key differences in cardiac non-myocytes between spontaneously type-2 diabetic (*db/db*) and healthy control (*db/h*) mouse hearts. Single-cell transcriptomic analysis revealed a concerted diabetes-induced cellular response contributing to cardiac remodeling. These included cell-specific activation of gene programs relating to fibroblast hyperplasia and cell migration, and dysregulation of pathways involving vascular homeostasis and protein folding. This work offers a new perspective for understanding the cellular mediators of diabetes-induced cardiac pathology, and pathways that may be targeted to address the cardiac complications associated with diabetes.

INTRODUCTION

Diabetes results in a significantly elevated risk of cardiovascular mortality and hospitalization for heart failure (HF).[1] Indeed, hyperglycemia alone is sufficient to induce cardiac dysfunction by multiple means, including oxidative stress, inflammation, and fibrosis.[2–4] Further, type-2 diabetes (T2D) is associated with an array of concomitant metabolic abnormalities including insulin resistance, dyslipidemia, hypertension, and obesity that further compound the risk and severity of cardiovascular disease in general, and of diabetes-induced heart failure in particular.[5,6] Treatment strategies to address diabetes-induced cardiac complications are limited, therefore understanding and targeting the precise molecular and cellular events that lead to pathological remodeling are required.

Whilst the specific impact of diabetes on cardiac myocytes has received considerable attention over recent decades,[7–10] relatively less is known of the impact of diabetes in cardiac non-myocytes, and their contribution to diabetes-induced cardiac remodeling.[11,12] Cardiac non-myocytes are present in greater numbers than myocytes and recent studies examining human heart and those of preclinical models, have highlighted the role of non-myocytes and their dynamics in health and disease contexts. Studies performed using single-cell omics methodologies have been particularly insightful, providing new cellular and molecular resolution of the network of cells that form the heart in homeostasis.[13,14] More recently, the utility of mouse models of cardiovascular disease underscore how the cellular networks are affected, uncovering novel cellular protagonists and molecular circuits driving cardiac pathology.[15,16] Despite this expanding knowledge, the impact of T2D on cardiac non-myocytes is yet to be examined at the single-cell resolution.

Here, we sought to address this gap in knowledge by determining the cellular and molecular changes in cardiac non-myocytes that accompany cardiac remodeling elicited by T2D. Single-cell transcriptomic analysis of 17-week old leptin-receptor deficient *db/db* mice and *db/h* heterozygote controls, revealed common and distinct cellular responses mediating diabetes-induced cardiac remodeling. These included

[1]Cardiac Cellular Systems, Baker Heart and Diabetes Institute, Prahran, VIC, Australia
[2]Preclinical Cardiology, Microsurgery and Imaging Platform, Baker Heart and Diabetes Institute, Prahran, VIC, Australia
[3]Heart Failure Pharmacology, Drug Discovery Biology, Monash Institute of Pharmaceutical Sciences, Parkville, VIC, Australia
[4]Department of Microbiology, Anatomy, Physiology and Pharmacology, La Trobe University, Bundoora, VIC, Australia
[5]Centre for Cardiovascular Biology and Disease Research, La Trobe University, Melbourne, VIC, Australia
[6]Baker Department of Cardiometabolic Health, University of Melbourne, Parkville, VIC, Australia
[7]Baker Department of Cardiovascular Research and Implementation, La Trobe University, Melbourne, VIC, Australia
[8]Department of Pharmacology, Monash University, Clayton, VIC, Australia
[9]These authors contributed equally
[10]Senior author
[11]Lead contact
*Correspondence: rebecca.ritchie@monash.edu (R.H.R.), alex.pinto@baker.edu.au (A.R.P.)
https://doi.org/10.1016/j.isci.2023.107759

the activation of well-established pathways associated with T2D, as well as new insights regarding the dynamics of the local cardiac microenvironment. Moreover, we also note a number of non-myocyte cellular alterations detected by flow cytometry in age-matched mice, which were associated with cell-specific transcriptomic perturbations. The findings from this study provide a framework for understanding the behavior of cardiac cell networks in T2D, and how specific nodes of these networks may be manipulated to ameliorate diabetes-associated cardiac disease.

Research design and methods

For a detailed description of the methodology, see the STAR Methods and supplemental information. All animal-related experiments were approved by the Alfred Research Alliance (ARA) Animal Ethics Committee (Ethics number: E/1880/2019/B) and were performed in accordance with the National Health and Medical Research Council of Australia (NH&MRC) guidelines. Male 10-week and 17-week-old *db/db* mice ([B6.BKS(D)-Lepr^{db}/J], stock #000697) and their heterozygous non-diabetic, age-matched littermate controls (*db/h*) were obtained from The Jackson Laboratory (Bar Harbor ME, USA,[17]). Sequencing data is publicly available at Array Express, accession number E-MTAB-11940. All scripts relating to this study are available upon reasonable request.

RESULTS

Male *db/db* mice recapitulate conventional markers of clinical type-2 diabetes

To determine the impact of murine T2D on cardiac non-myocytes, we utilized the *db/db* spontaneous mouse model of diabetes, whereby mice display hyperglycemia from four-weeks of age.[17] Progression of cardiac remodeling and subsequent impairments in cardiac function as a result of diabetes are generally evident later than the onset of hyperglycemia in murine models.[9,18] To capture the cardiac cellular and molecular events that are altered with diabetes, where diastolic dysfunction is detectable, we selected 17 week-old *db/db* diabetic and *db/h* control mice for analysis. Confirming the presence of systemic T2D, blood glucose levels and body weight were significantly elevated throughout the duration of the study (Figures S1C and S1D), corroborated by higher glycated hemoglobin (% HbA1c), and increased body weight and fat mass in *db/db* mice, relative to *db/h* controls (Figures S1E–S1H). In addition, we confirmed *db/db* mice exhibited impaired left ventricle (LV) diastolic function compared to *db/h* mice (Figure S2). Using tissue Doppler and pulsed-wave Doppler echocardiography, we detected significantly reduced e' velocity, with an increased E/e' ratio (Figures S2C and S2D), which has been associated with impaired left-ventricular filling pressure.[19,20] Indeed, the E/e' ratio is currently considered the most robust echocardiography-derived index of LV diastolic function.[2,20] Moreover, M-mode echocardiography of left-ventricular chamber sizes and wall thickness indicated reduced end-diastolic and systolic dimensions in *db/db* mice, which was accompanied by an enhanced fractional shortening relative to *db/h* littermates (Figures S2E and S2F). Postmortem analyses revealed augmented lipid content in the myocardium, detected by Oil red O staining (Figures S1A and S1B). Using whole blood flow cytometry, we noted no differences between circulating leukocytes in *db/db* and *db/h* mice at 10-week of age (Figures S1I–S1K). However, we did observe increased levels of circulating monocytes and neutrophils in 17-week old *db/db* mice, despite no apparent differences in lymphocyte numbers, relative to their control counterparts (Figure S1L–S1M). These observations are congruent with phenotypic characteristics of murine T2D previously described by others.[17,21–23]

Single-cell transcriptomic mapping of non-myocytes in in the *db/db* and *db/h* mouse hearts

Given that murine T2D alters systemic and cardiac functional parameters in 17 week-old mice, we next sought to determine potential cellular bases for these changes by examining transcriptomic perturbations in non-myocytes of diabetic hearts using scRNA-seq (Figures 1A and 1B). To limit the impact of potential outliers, we pooled single-cell suspensions from four *db/h* control mouse hearts and four *db/db* mouse hearts to prepare two 10X Genomics 3′ Single-cell Transcriptome libraries (See STAR Methods). To further minimize batch effect artifacts, we prepared single-cell suspensions and transcriptomic libraries of *db/h* and *db/db* mouse heart cells in parallel (on the same day), in addition to performing data normalization implemented by the Seurat data analysis package (See STAR Methods). Our analysis yielded a comprehensive atlas of cardiac non-myocytes capturing a wide array of cell types in both *db/db* and *db/h* mice (7,811 cells, Figures 1C and 1D). Unbiased determination of genes most-highly enriched for each cell cluster identified the populations of cells analyzed (Figure 1E). These included fibroblasts (*Clec3b, Dpep1*), pericytes (*Vtn, Kcnj8*), endothelial cells (ECs; *Cd36, Ly6c1*), smooth muscle cells (SMCs; *Myh11, Acta2*), endocardial cells (*H19, Tmem108*), epicardial cells (*Upk3b, Msln*), and a number of immune cells including macrophages, B-cells, T-cells, eosinophils/basophils, DC-like cells and granulocytes (Figures 1C–1E). Other cell types included γδT-cells (*Cd3g*), NK-cells (*Nkg7*), and Schwann cells (*Kcna1*). Cell types were also confirmed by querying established marker genes (Figure S3; Table S1).

Cell-specific shifts in gene expression induced by diabetes

Next, we sought to identify how murine T2D alters cellular gene expression in cardiac non-myocytes. Comparing cells from *db/db* and *db/h* hearts, we found significant cell-specific changes in gene expression (Figure 2). Examination of the top genes upregulated for each major cardiac cell population identified many that have been previously implicated in diabetes or obesity (Figure 2A; Table S2). These included: nutrient partitioning ligand *Angptl4*,[24] which was increased specifically in *db/db* fibroblast populations, as well as metabolic transcriptional regulator *Pparγ* specific to ECs (Table S3).[25] We also found increased transcript levels of the chemotactic receptor *Ccr2* (Figure 2A), and, to a lesser extent, chemotaxis-regulating secreted factor genes *S100a4* and

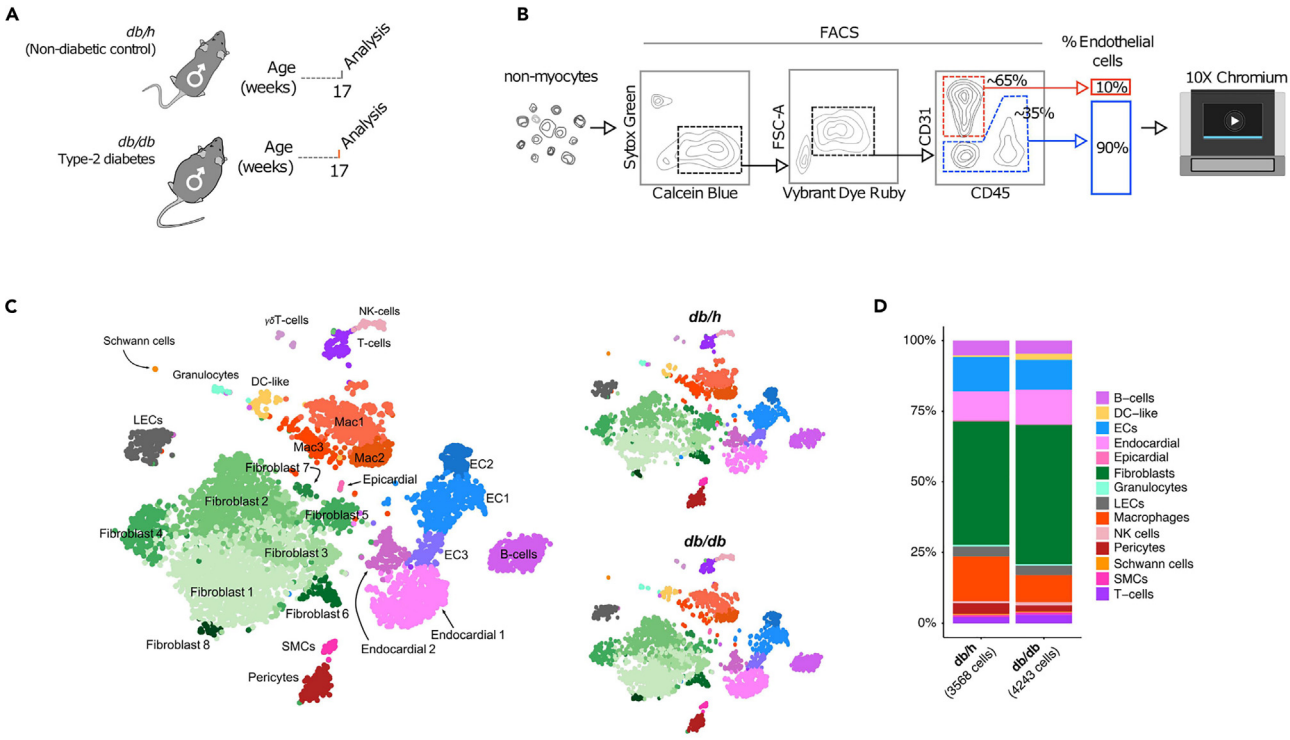

Figure 1. Analysis of the T2D (*db/db*) mouse heart cellulome

(A and B) Schematic indicating the analyses conducted on the *db/db* and *db/h* mouse hearts. Single-cell RNA sequencing was performed in 17-week old male *db/db* (n = 4) and *db/h* (n = 3) mouse hearts, as previously described.[15]

(C) Merged t-SNE projection of all captured cardiac non-myocyte cells with adjacent split tSNE projections from *db/h* and *db/db* mice.

(D) Barplot summarising relative abundances of major cell types represented in the single-cell RNA sequencing dataset.

(E) Dot plot illustrating the top-5 most highly expressed genes within each cell cluster. Dot size indicates the relative proportions of cells expressing a given gene and dot color indicates the relative average expression level.

S100a6[26,27] specifically in *db/db* cardiac macrophages (Tables S2 and S3). Intriguingly, the most consistent and robust gene increased in expression level across multiple cell types corresponded to the long non-coding RNA (lncRNA) gene *Gm11867* (Figure 2A), of which little is known. Conversely, top downregulated genes are primarily characterised by genes corresponding to heat shock proteins (*Hspa1a*, *Hspa1b*, *Hsbp1*, *Hsp90aa/b1*) as well as other protein folding-related genes (*Ahsa1*, *Asha2*, *Dnaja1*, *Serpinh1*, *Stip1*), which were most markedly downregulated in vascular cells, such as endothelial cells, pericytes, SMCs and lymphatic ECs (LECs). Additionally, among the top downregulated genes in DC-like cells and macrophages were complement proteins *C1qa*, *b* and *c* (Figure 2B; Tables S2 and S3), which are involved in opsonization and dampening of inflammation.[28]

To determine the coherent gene expression programs that are altered in non-myocytes from *db/db* mouse hearts, we performed gene ontology (GO) analysis of these differentially expressed genes (Figures 2C and 2D). Endothelial cells and fibroblasts displayed the most significantly upregulated gene programs in our dataset. These primarily included pathways involving organ and cellular

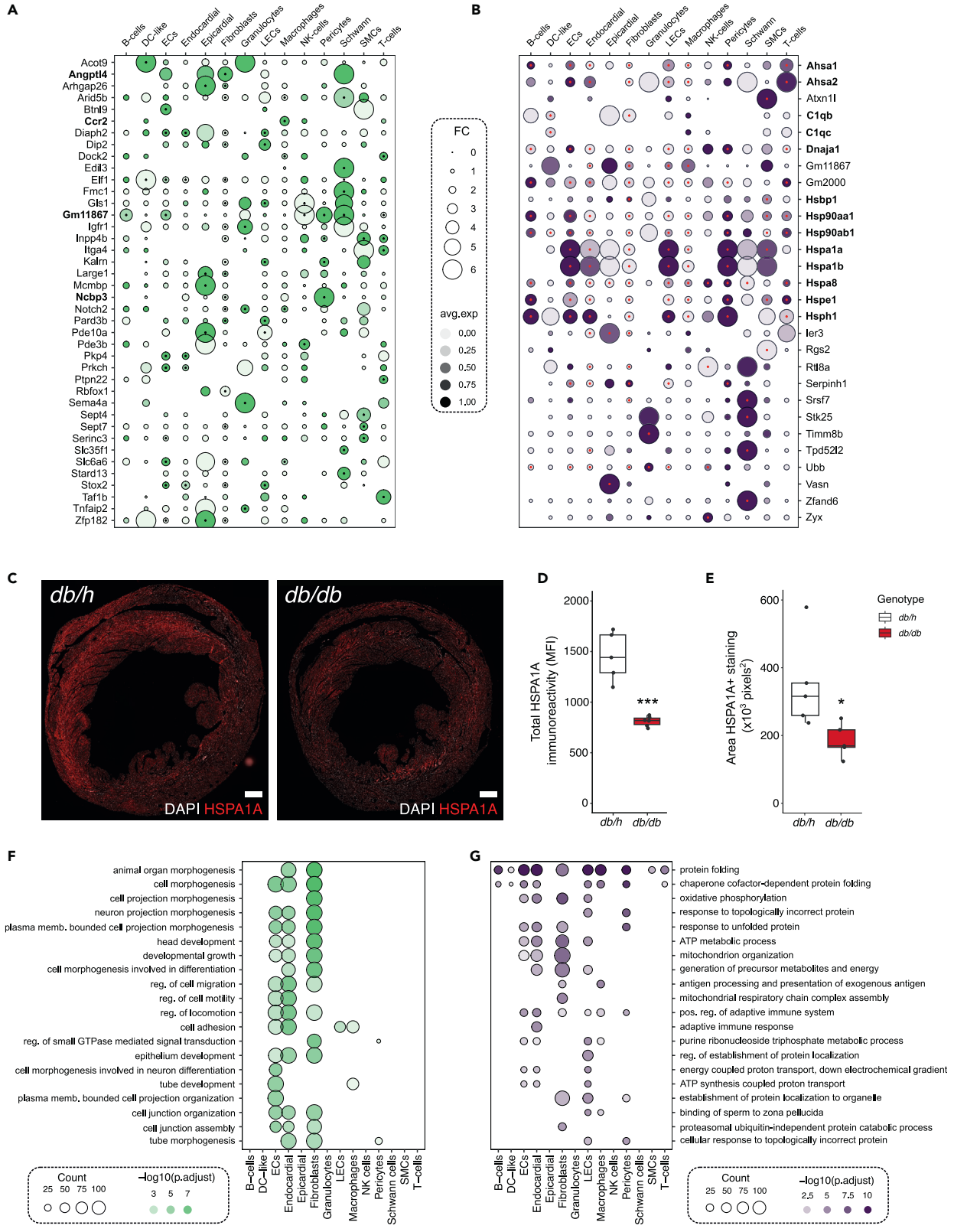
A
B-cells
DC-like
ECs
Endocardial
Epicardial
Fibroblasts
Granulocytes
LECs
Macrophages
NK-cells
Pericytes
Schwann
SMCs
T-cells
Acot9
Angptl4
Arhgap26
Arid5b
Btnl9
Ccr2
Diaph2
Dip2
Dock2
Edil3
Elf1
Fmc1
Gls1
Gm11867
Igfr1
Inpp4b
Itga4
Kalrn
Large1
Mcmbp
Ncbp3
Notch2
Pard3b
Pde10a
Pde3b
Pkp4
Prkch
Ptpn22
Rbfox1
Sema4a
Sept4
Sept7
Serinc3
Slc35f1
Slc6a6
Stard13
Stox2
Taf1b
Tnfaip2
Zfp182
FC
0
1
2
3
4
5
6
avg.exp
0.00
0.25
0.50
0.75
1.00
B
Ahsa1
Ahsa2
Atxn1l
C1qb
C1qc
Dnaja1
Gm11867
Gm2000
Hsbp1
Hsp90aa1
Hsp90ab1
Hspa1a
Hspa1b
Hspa8
Hspe1
Hsph1
Ier3
Rgs2
Rtl8a
Serpinh1
Srsf7
Stk25
Timm8b
Tpd52l2
Ubb
Vasn
Zfand6
Zyx
C
db/h
DAPI HSPA1A
db/db
DAPI HSPA1A
D
Total HSPA1A immunoreactivity (MFI)
2000
1500
1000
500
0
***
db/h
db/db
E
Area HSPA1A+ staining (x10³ pixels²)
600
400
200
0
*
db/h
db/db
Genotype
db/h
db/db
F
animal organ morphogenesis
cell morphogenesis
cell projection morphogenesis
neuron projection morphogenesis
plasma memb. bounded cell projection morphogenesis
head development
developmental growth
cell morphogenesis involved in differentiation
reg. of cell migration
reg. of cell motility
reg. of locomotion
cell adhesion
reg. of small GTPase mediated signal transduction
epithelium development
cell morphogenesis involved in neuron differentiation
tube development
plasma memb. bounded cell projection organization
cell junction organization
cell junction assembly
tube morphogenesis
B-cells
DC-like
ECs
Endocardial
Epicardial
Fibroblasts
Granulocytes
LECs
Macrophages
NK cells
Pericytes
Schwann cells
SMCs
T-cells
Count
25 50 75 100
−log10(p.adjust)
3 5 7
G
protein folding
chaperone cofactor-dependent protein folding
oxidative phosphorylation
response to topologically incorrect protein
response to unfolded protein
ATP metabolic process
mitochondrion organization
generation of precursor metabolites and energy
antigen processing and presentation of exogenous antigen
mitochondrial respiratory chain complex assembly
pos. reg. of adaptive immune system
adaptive immune response
purine ribonucleoside triphosphate metabolic process
reg. of establishment of protein localization
energy coupled proton transport, down electrochemical gradient
ATP synthesis coupled proton transport
establishment of protein localization to organelle
binding of sperm to zona pellucida
proteasomal ubiquitin-independent protein catabolic process
cellular response to topologically incorrect protein
B-cells
DC-like
ECs
Endocardial
Epicardial
Fibroblasts
Granulocytes
LECs
Macrophages
NK cells
Pericytes
Schwann cells
SMCs
T-cells
Count
25 50 75 100
−log10(p.adjust)
2.5 5 7.5 10

Figure 2. Differentially expressed genes in the *db/db* heart

(A) Dot plot illustrating the top upregulated genes in *db/db* hearts relative to *db/h* counterparts.

(B) Downregulated gene expression patterns within *db/db* hearts relative to *db/h* counterparts. Dot color is relative to the average expression within each cell cluster (green = upregulated, purple = downregulated). Dot size indicates fold change in *db/db* non-myocyte cells relative to *db/h* control cells. Points within the center of colored dots indicate a statistical difference in gene expression in *db/db* hearts relative to *db/h* controls (uncorrected $p < 0.0001$).

(C) Representative cardiac cross-sections of *db/db* and *db/h* hearts (Scale bar = 475μm).

(D and E) Quantified immunoreactivity of HSPA1A in *db/db* and *db/h* heart sections.

(F and G) Dot plots illustrating the top-3 gene ontology (GO) terms for upregulated genes and downregulated genes, respectively, in each broad cell type (corrected $p < 0.05$). For GO terms, circle size indicates the number of genes corresponding to a given term and color intensity indicates statistical significance (*p.adjust*). See corresponding Tables S2 and S3 for additional information relating to differentially expressed genes.

morphogenesis (Figures 2C; Table S4). Exhibiting signs of vascular remodeling, cardiac ECs upregulated programs involved in angiogenesis such as *tube development* and *blood vessel development* in *db/db* mice. Genes upregulated in ECs were also enriched for *neuron projection development*, indicating possible compensatory mechanisms for axonal degeneration, observed in clinical T2D.[29] Finally, genes corresponding to the positive regulation of GTPase activity were enriched in fibroblasts. These genes—which included *Cdc42se* and other G-protein coupled receptor genes—are likely to mediate mitogen-activated protein kinase (MAPK) related signaling.[30] Conversely, we found near-universal downregulation of programs corresponding to *protein folding* (Figure 2D) in almost all cell types. Moreover, downregulated gene programs also corresponded to *response to unfolded protein response*, comprising the core heat shock proteins aforementioned.

Diabetes is associated with increased ligand and receptor expression in cardiac non-myocytes

In addition to the cell-specific changes described above, we hypothesized that T2D also alters cardiac paracrine communication networks. To examine this, we quantified shifts in ligand-receptor expression using the CellPhoneDb resource.[31] Initially, we mapped the net intercellular connections between cardiac non-myocyte cell populations from *db/h* and *db/db* mice, revealing increased cardiac intercellular communication, among all cell types (Figures 3A and 3B). As identified previously,[14,15] we found that fibroblasts exhibit the greatest number of total intercellular connections in our dataset (Figure 3B). Next, we examined differentially expressed genes encoding endogenous ligands and their cognate receptors that were most significantly up or downregulated in *db/db* mouse hearts (Figures 3C–3F; Tables S5 and S6). Top upregulated ligand genes existed primarily within fibroblasts (Figure 3C), corresponding to *extracellular matrix organization*, and *extracellular structure organization*. While our dataset indicated increased levels of transcripts corresponding to *Col14a1*, *Col5a2* and others in *db/db* fibroblasts (Figures 3C; Table S6), the modest increase in fibrogenic ligand genes was insufficient to yield detectable histological changes in cardiac fibrosis in 17-week old *db/db* mice (Figure S4). Other pathways corresponding to upregulated ligands in *db/db* mice include *negative regulation of cell development*, *angiogenesis*, and *tube formation*. Top programs corresponding to upregulated receptors primarily included those involved in vascular remodeling, including *angiogenesis*, *vasculogenesis*, and *ameboidal-type cell migration* (in fibroblasts and to a lesser extent in ECs, Figure 3D). Angiogenesis-related receptor genes enriched in endothelial cells included: membrane repair protein gene *Dysf*; the vascular endothelial cell growth factor receptors *Kdr*, *Flt1*, and *Nrp1*; TGFβ-family-associated genes *Eng* and *Tgfbr2*; and the scavenger receptor *Cd36* (Table S5; specific examples shown in Figure S5). Endothelial cells, endocardial cells, fibroblasts, and macrophages also upregulated receptors involved in chemotaxis (Figure 3D). These included the upregulation of genes linked to *negative regulation of chemotaxis*, such as: *Dysf*,[32] *Eng*,[33] *Ptprm*[34] in ECs, also accompanied by genes associated with *angiogenesis*, including *Kdr*, *Flt1*, and *Nrp1* in ECs). Among the top upregulated receptors, were those corresponding to *positive regulation of MAPK cascade* (Figure 3D). Key genes corresponding to MAPK included insulin receptors *Insr*, *Igf1r*, and *Tgfbr1* in fibroblasts, *Egfr* in both fibroblasts and macrophages, and *Cd36* in macrophages and pericytes (Table S5).

The most significant pathways downregulated among cardiac cells were also related to MAPK signaling. Ligand genes forming *ERK1 and ERK2 cascade* (for example, *Apoe* and *Timp3*) were highly enriched in macrophages and, to a lesser extent, in fibroblasts (Figures 3E; Table S6). Fibroblasts also downregulated receptor genes involved in the *positive regulation of MAPK cascade* (including, *Cd74* and *Ret*; Figures 3F; Tables S5 and S6).

However, the most significant and broadly downregulated gene expression patterns involved those associated with leukocyte trafficking, indicating a concerted cellular response by cardiac non-myocytes to dampen inflammation. This included the downregulation of ligand gene programs corresponding to leukocyte migration (*lymphocyte migration* and *leukocyte chemotaxis*) primarily by macrophages (Figure 3E). Key downregulated ligands included: endoplasmic reticulum protein *Calr* (in LECs, endocardial cells and fibroblasts), that when interstitially localised, activates DCs and macrophages[35]; and *Anxa1* in LECs and endocardial cells. Macrophages also downregulated inflammatory mediators *Ccl4*, and *Il1b* (Table S8). Other important downregulated genes included complement components 7 and 4b (*C7* and *C4b*, respectively), which were reduced by the greatest magnitude within fibroblast sub-clusters 1 and 2 from *db/db* mice (Table S3). Meanwhile, the most significantly downregulated receptor programs were within pericytes, which had reduced levels of transcripts corresponding to *Cd74*, *Cd81*, and *Il2ra* (Figure 3F), further implicating perturbed vascular cell migration. *Cd74* and *Cd81* were also reduced in expression in a range of other cells, including fibroblasts and macrophages (Table S3).

Murine type-2 diabetes alters the proportions of cardiac non-myocytes

The alteration in gene programs involved in cell trafficking and intercellular signaling, in addition to findings from our previous study in an alternative murine model of type 2 diabetes,[12] suggest that diabetes alters relative cardiac cellular abundances. Analysis of cell numbers

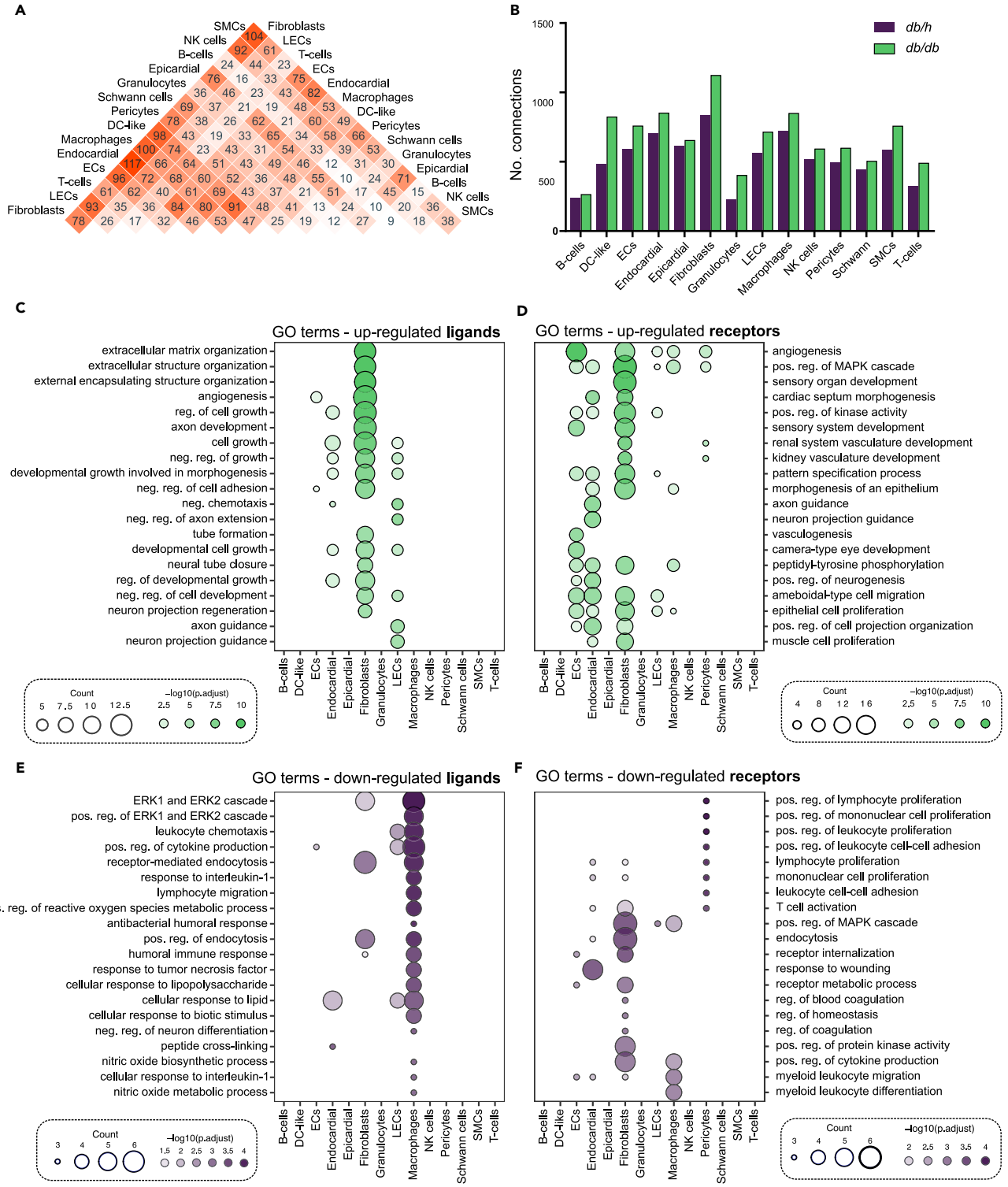

Figure 3. Intercellular communication is increased in the *db/db* heart

(A) Heatmap indicating the number of cell-cell interactions in *db/db* hearts, determined by CellphoneDB analysis. Color intensity and values within the boxes indicate the number of connections between individual cell populations.

(B) Bar plot showing the net cellular interactions in each major cell type in *db/h* and *db/db* hearts.

(C and D) GO terms enriched in genes corresponding to upregulated ligands (C) and upregulated receptors (D) in *db/db* hearts, relative to *db/h* controls.

(E and F) GO terms enriched in genes corresponding to (E) downregulated ligands and (F) downregulated receptors, in *db/db* hearts relative to *db/h* controls. Circle size indicates the number of genes corresponding to a given GO term and color intensity indicates statistical significance ($p < 0.01$).

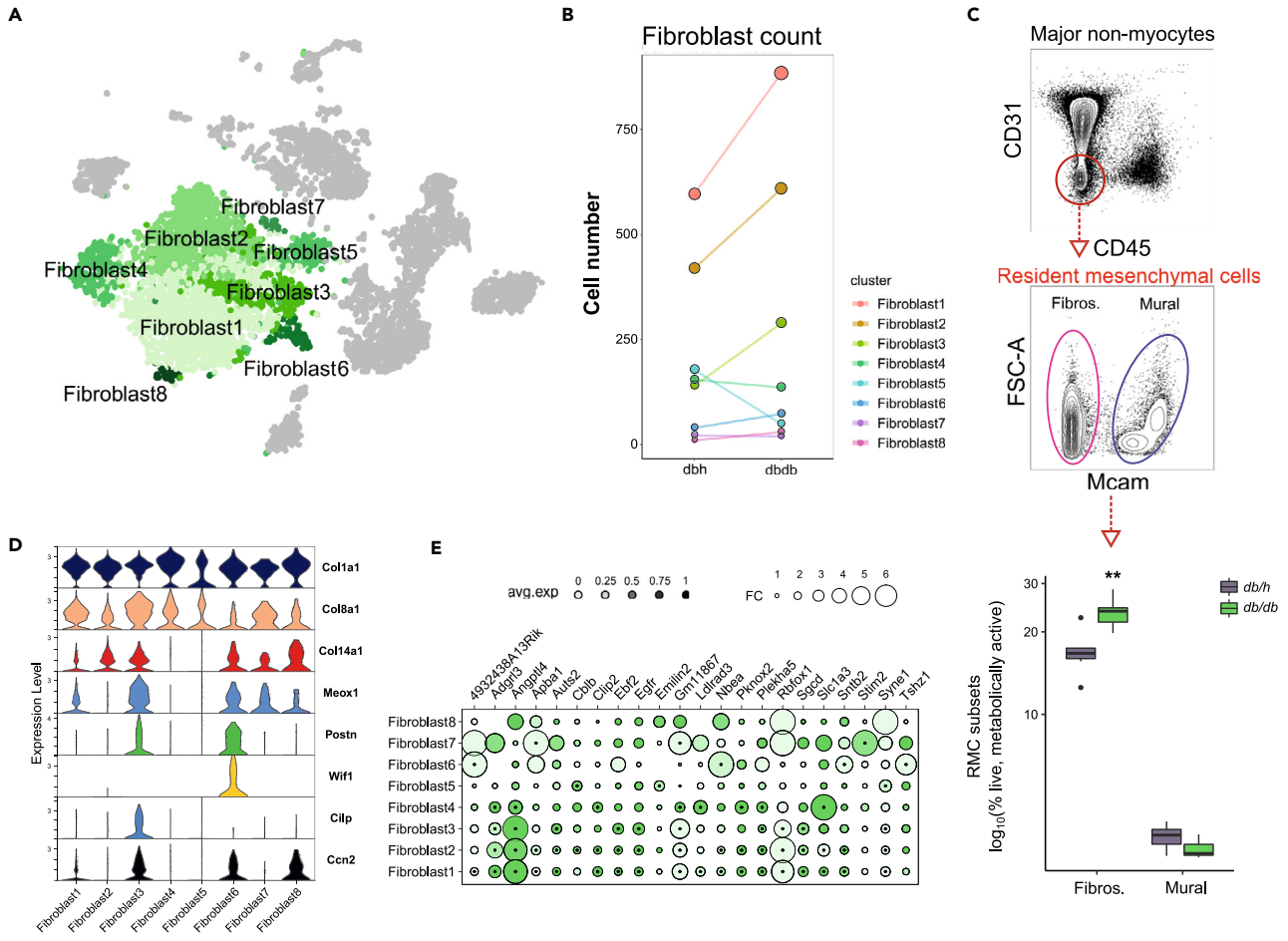

Figure 4. Analysis of cardiac fibroblasts in the *db/db* heart

(A) Merged tSNE plot highlighting cardiac fibroblasts relative to other cardiac non-myocytes.

(B) Number of cells within each cardiac fibroblast sub-cluster in *db/h* and *db/db* mice.

(C) Flow cytometry gating strategies employed for the selection of fibroblasts and mural cells in an age-matched cohort of *db/h* and *db/db* mice. Quantified flow cytometry data corresponding to gating strategies above (n = 8/group). Flow cytometry data was analyzed statistically using the Wilcoxon rank-sum test to determine differences between groups. This data is presented as median ±SD, **p < 0.01.

(D) Violin plot of distinct marker genes within each fibroblast sub-cluster.

(E) Top-3 differentially expressed genes within each fibroblast cluster in *db/db* mice, relative to *db/h* controls. Dot color and size are proportional to average expression and fold change, respectively, within each cell cluster. Black points located within the center of some circles indicate a significant difference in gene expression in *db/db* mice compared to *db/h* mice (uncorrected p < 0.01).

in our scRNA-seq dataset suggested shifts in the abundance of multiple cell subsets, and in particular, fibroblasts (Figures 4A and 4B). To confirm this, we performed flow cytometric quantification of resident mesenchymal cells (RMCs) within cardiac non-myocytes from *db/h* and *db/db* mice at both 10 and 17-week of age. While 10-week old mice displayed no differences in fibroblast levels (Figure S6B), we found a higher proportion of fibroblasts in *db/db* mouse hearts relative to *db/h* mice at 17-week of age (Figures 4C and S6C). Driving these increases in fibroblasts, were fibroblast sub-clusters 1, 2 and 3 within our scRNA-seq dataset (Figure 4B). Therefore, we next analyzed these specific fibroblast cell subsets in more detail to determine their impact within the cardiac cellulome (Figures 4D and 4E). Examination of distinct genes between fibroblast subsets, found that Fibroblast 3 highly expresses *Cilp*, which we have previously identified as a highly fibrogenic, activated fibroblast subtype (termed "Fibroblast-*Cilp*") following angiotensin II (AngII) infusion (Figure 4D).[15] Analogous to the Fibroblast-*Cilp* population in our previous study, Fibroblast 3 displayed high levels of transcripts corresponding to pro-fibrotic genes including *Postn*, *Meox1*, *Ccn2* and exhibited increased levels of *Col8a1* relative to other fibroblast clusters (Figure 4D). However, while cardiac fibroblasts increased in proportion in 17-week old *db/db* mice, as mentioned they did not display overt cardiac fibrosis (Figure S4), nor increased levels of *Col1a1*—encoding a major component of extracellular matrix (ECM) that is elevated in expression in fibrosis,[36] relative to *db/h* mice (Figure 4E). Furthermore, transcriptomic comparison of genes enriched in Fibroblast clusters 1, 2 or 3 did not show display significant GO pathways related to fibrosis in any subset, relative to all other fibroblast subtypes (Figures S6D–S6F; Table S7; *p.adjust* = NS).

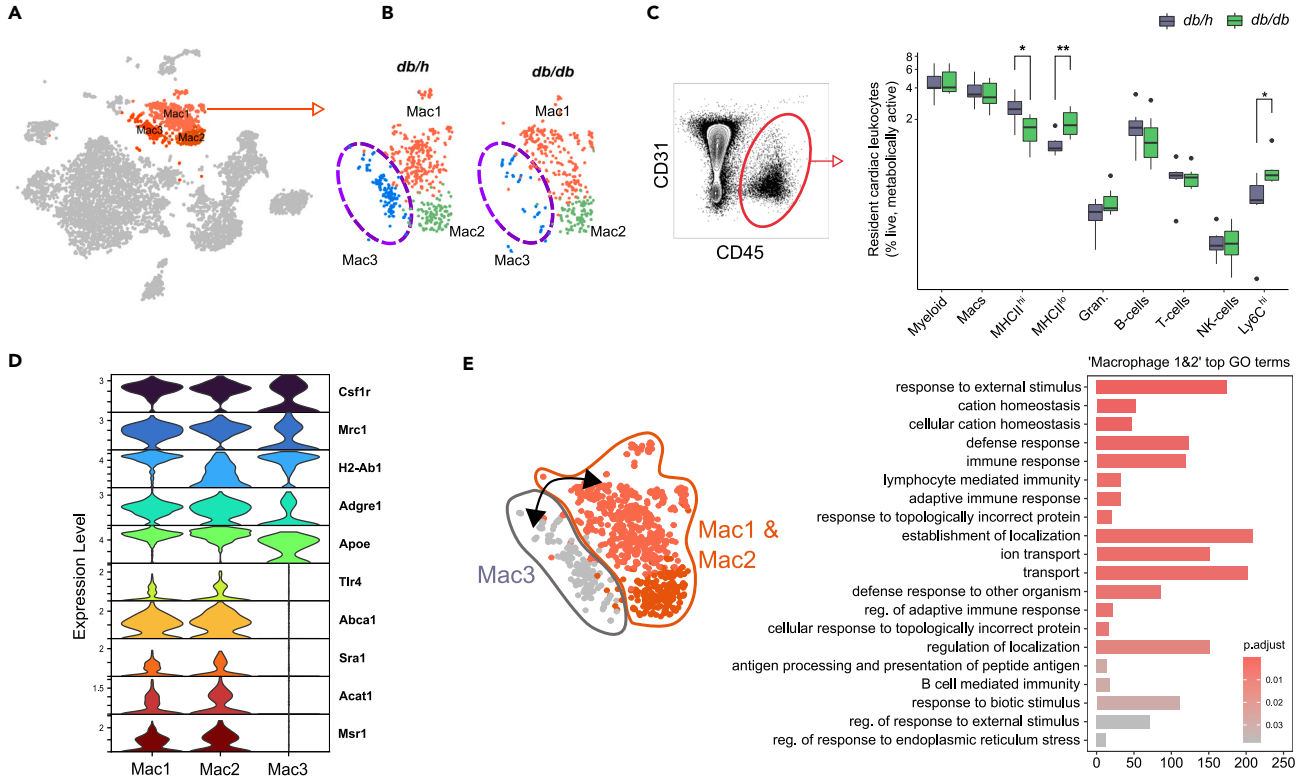

Figure 5. A subset of cardiac resident macrophages are lost in *db/db* hearts

(A) Merged tSNE plot highlighting cardiac macrophages, relative to other cardiac non-myocyte cells.

(B) tSNE projection of *in silico* isolated macrophages, in *db/h* and *db/db* mouse hearts.

(C) Flow cytometry gating strategy for selecting cardiac leukocytes with adjacent quantified results of various cardiac leukocyte subtypes analyzed. Flow cytometry data was analyzed statistically using the Wilcoxon rank-sum test to determine differences between the groups. This data is presented as median ±SD, *p < 0.05, **p < 0.01. Macs = macrophages, MHCII^{hi} = MHCII "high" macrophages, MHCII^{lo} = MHCII "low" macrophages, Gran. = granulocytes, Ly6C^{hi} = Ly6C "high" monocytes.

(D) Violin-plot mapping established macrophage markers, as well as critical reverse cholesterol/lipid transporters.

(E) GO analysis of distinct genes in Macrophage clusters 1 and 2, relative to Macrophage 3. Bar plot lists the top 20 GO terms enriched in genes from Macrophage 1 and 2, compared to Macrophage 3. The x axis indicates the number of genes mapped to a given GO term, which themselves are displayed on the y axis. Bar color indicates the adjusted p value ("p.adjust") from *in silico* GO enrichment analysis.

Another cell population with altered cell proportions following murine T2D, were cardiac macrophages. Analysis of macrophage subset abundances found that Macrophage 3 was almost completely depleted in *db/db* mouse hearts (Figures 5A and 5B). Both Macrophage 3 and Macrophage 1 constitute macrophage subsets with high levels of transcripts corresponding to *H2-Ab1* and *H2-Aa* genes, encoding the major histocompatibility complex II (MHCII) receptor (Figure 5D). Confirming the changes in macrophage subpopulation abundance, cardiac flow cytometric analyses from age-matched 17-week old mice found MHCII^{hi} macrophages were indeed reduced in proportion (Figure 5C). Moreover, we also noted an increase in Ly6C^{hi} monocytes by flow cytometry in age-matched *db/db* mouse hearts (Figures 5C; Figure S6C), consistent with their increase in circulation (Figure S1L–S1M).

To determine potential mechanisms for decreased macrophages we examined key genes within Macrophage 3 that may lead to their reduction. While Macrophage 3 was enriched for macrophage-related genes such as *Csf1r*, *Mrc1* and *H2-Ab1*, we found they had reduced or very low expression of genes associated with reverse cholesterol and lipid transport. These included *Apoe*, *Tlr4*, *Abca1*, *Sra1*, *Acat1* and *Msr1* (Figure 5D). Corroborating this pattern, GO analysis performed from genes distinct to Macrophage 1 and 2, relative to genes in Macrophage 3, identify terms corresponding to *transport, response to external stimulus* and *defense response* (Figures 5E; Table S8). Indeed, transcripts encoded reverse cholesterol transport receptors, were among top genes distinguishing Macrophage 1 and 2 from Macrophage 3 (Table S8). Therefore, these observations suggest the lack of cellular machinery to expel excess intracellular cholesterol is one possible mechanism by which Macrophage 3 subset is lost in *db/db* mouse hearts.

Identifying common molecular pathways in the diabetic heart

Considering the array of altered pathways identified in *db/db* hearts, we next sought to systematically determine common genes that are dysregulated in the diabetic heart by analyzing our scRNA-seq data in conjunction with data from unaffiliated studies examining

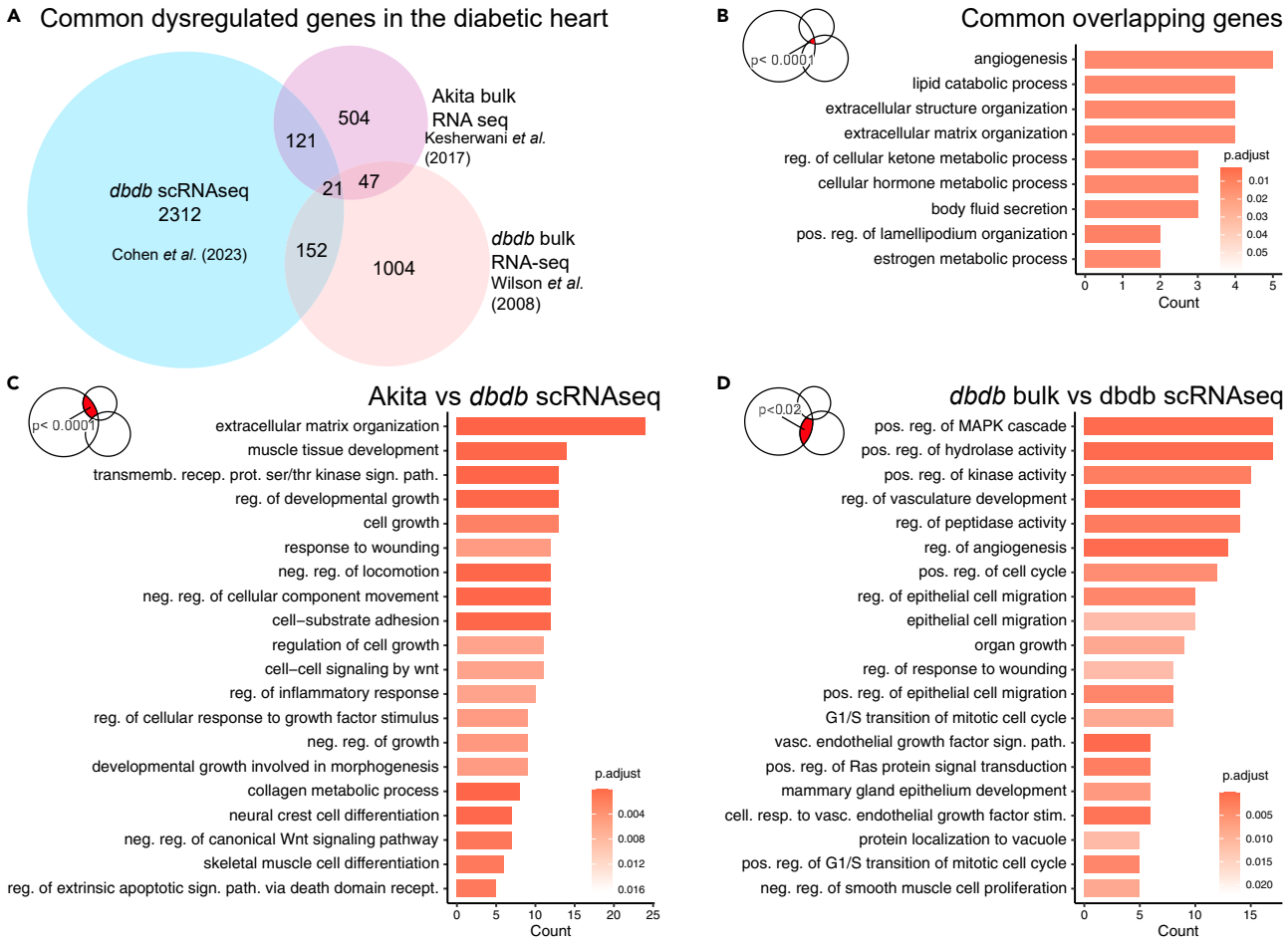

Figure 6. Integration of unaffiliated bulk RNA sequencing datasets highlights common molecular pathways in the diabetic heart

(A) Proportional Venn diagram illustrating unique and common differentially expressed genes in our scRNA-seq dataset relative to two publicly available bulk RNAseq datasets of the diabetic heart.

(B) Between all datasets analyzed, there were 21 common genes. Gene lists were derived from each overlap and subsequently underwent GO enrichment analysis. GO analysis revealed the top 20 common biological functions (y axis) and the collection of genes corresponding to each GO term (x axis).

(C) GO analysis of bulk RNA-seq genes in the T1D Akita mouse heart relative to our *db/db* scRNA-seq dataset.

(D) GO analysis pertaining to common genes in the *db/db* bulk RNAseq dataset compared to the *db/db* scRNA-seq dataset, highlighting key non-myocyte differentially expressed genes. The hypergeometric p values displayed in B-D correspond to the statistical significance of the overlaps between gene sets (highlighted in red). Datasets were obtained from the Gene Expression Omnibus (GEO) repository. "Akita" dataset identifier: GSE66577. Bulk RNAseq *db/db* dataset identifier: GSE36875.

diabetes-induced cardiac remodeling. To achieve this, we compared differentially expressed genes of cardiac non-myocytes from our scRNA-seq analysis, with differentially expressed genes within cardiac bulk RNA-seq datasets from 12-week-old "Akita" (*Ins*^{2Akita}) mice (*Gene Expression Omnibus* accession number GSE66577) and 13 week-old *db/db* mice (GSE36875). While both *db/db* datasets analyzed represent characteristics of T2D, Akita mice—bearing a single base pair substitution in the *Ins2* gene—exhibit features of type 1 diabetes.[37] Comparison of all datasets showed both common and distinct differentially regulated gene networks. Given bulk-RNA analysis data is primarily composed of RNA derived from myocytes, and our dataset is focused on non-myocyte populations, a limited number of common genes were observed between scRNA-seq and bulk RNA datasets. Nevertheless, we found 21 overlapping genes in all three datasets (Figure 6A; Table S9). These corresponded to programs such as ECM remodeling (four genes: *Spock2, Adamts2, Cyp1b1* and *Col23a1*), lipid catabolism (five genes: *Cpt1a, Hsd17b11, Enpp2* and *Cyp1b1*), and angiogenesis (three genes: *Aqp1, Enpp2* and *Cyp1b1*, Figures 6B; Table S9). Comparison of scRNA-seq genes with differentially expressed genes from Akita mouse hearts identified a greater number of genes corresponding to *extracellular matrix organization* (23 genes: including, *Lum, Col1a2, Postn* and *Serpine1*), *negative regulation of cell migration* (12 genes, for example: *Serpine1, Apoe, Il33* and *Emilin1*) and *muscle tissue growth* (14 genes: for example, *Igf2, Plag1* and *Eln*, Figures 6C; Table S9). Meanwhile, top programs identified as dysregulated in our scRNA-seq dataset, and bulk RNA-seq analysis of *db/db* mouse heart tissue, included those relating to *positive regulation of MAPK cascade* (16 genes, for

example, *Ptprc*, *Map4k4*, *Pdgfra* and *Cd74*), *regulation of angiogenesis* (13 genes: for example, *Btg1*, *Pparγ*, *Ets1* and *Pgf*) and *leukocyte migration* (12 genes: including, *Cd9*, *Kitl*, *Il16*, *Ccl11*, Figures 6D; Table S9). These observations underscore that ECM and vascular remodeling, accompanied by aberrant MAPK signaling are common and key features of pathological remodeling elicited by *db/db*-induced T2D.

DISCUSSION

While cardiovascular complications associated with diabetes have been studied for decades, the specific cellular and molecular events dictating the development and progression of heart failure remain poorly understood, particularly beyond the cardiac myocyte. Here, we used a single-cell omics approach to study cardiac non-myocytes, in the most widely used mouse model of T2D the leptin-receptor *db/db* mutant mouse.[5,17,38] The key motivation for this was the paucity of data examining the roles of disparate cardiac non-myocytes in cardiac remodeling induced by diabetes. We also noted that mice with T2D exhibited early signs of cardiac dysfunction, allowing us to capture the relevant cellular and molecular events driving cardiac remodeling in murine T2D. Further, profiling of the diverse network of non-myocytes that comprise the heart in diabetes has not been performed using high-resolution transcriptomics. Our study found that virtually all cell populations within the heart are affected by murine T2D, which alters the cardiac cellular landscape at both the gene expression and cell abundance levels. Importantly, these marked changes in the molecular and cellular profile of the diabetic myocardium precede, and hence likely drive, clinically significant diabetes-induced adverse cardiac remodeling.

Within the cardiac mesenchymal cell compartment, we found increased fibroblast levels in *db/db* hearts accompanied by significant gene expression changes. This included the expansion of three fibroblast subsets (Fibroblast 1, 2 and 3). While the phenotypes of Fibroblast 1 and 2 were similar from their gene expression profiles, Fibroblast 3 cells corresponded to those enriched in the matricellular protein gene *Cilp*, which we have previously found to be highly fibrogenic in an AngII model of fibrosis.[15] In addition to *Cilp*, Fibroblast 3 expresses other markers of fibrogenic fibroblasts, such as *Postn*, *Ccn2* and *Meox1*. In particular, *Meox1* was recently identified as a transcriptional "switch" in activated fibroblasts that regulates fibroblast phenotypes and governs fibrosis.[16] Despite this and the observation of mild diastolic dysfunction in *db/db* mice in this study, we did not detect a significantly higher level of transcripts corresponding to key fibrosis-related genes, such as *Col1a1*, in any fibroblast subtype. Although fibroblast hyperplasia is evident, lack of fibrosis was further confirmed histologically. This suggests that additional molecular circuits may be required to induce fibrogenic phenotypes of fibroblasts and extensive fibrosis, as seen at later time points in the *db/db* mouse model.[22] As such, diastolic dysfunction seen here—at the nascent stages of cardiomyopathy development—may primarily have myocentric origins.[39–41] However, we did observe increased levels of transcripts for ECM-related genes within expanding fibroblast subsets, suggesting the commencement of cardiac fibrotic remodeling. In addition, we noted that dysregulated genes common to both our study and unaffiliated bulk transcriptomic studies examining Akita[42] and *db/db* mouse hearts[43] include those involved in ECM remodeling, further suggesting cardiac fibrosis in 17-week old *db/db* mice, may be at early stages of development.

Another prominent feature of maladaptive cardiac remodeling in this study—particularly among vascular cells—was the downregulation of genes relating to heat shock proteins (HSPs). HSPs have a number of cytoprotective roles, including antioxidant, protein folding, and anti-apoptotic activity.[44–46] We found HSP70 and HSP90 family members (encoded by *Hspa1a*, *Hspa1b*, *Dnaja1*, and *Hsp90aa/b1*, *Ahsa1/2* genes, respectively), were most markedly reduced in ECs, LECs, SMCs and, to a greater extent, pericytes. Endocardial cells and fibroblasts also exhibited attenuated transcript levels corresponding to these genes, albeit at a reduced magnitude. Consistent with this, diabetes induces the downregulation of HSP gene expression in striated muscle,[47,48] while exercise conversely upregulates HSP gene and protein expression,[49–51] implying that HSP expression is proportional to insulin sensitivity. Whether HSPs directly contribute to insulin resistance or if this paradigm is secondary to the myriad of perturbations in T2D, remains to be determined. Notwithstanding, this study provides new cell-specific information regarding HSP behavior in cardiac non-myocytes, suggesting these molecules play an important role in vascular homeostasis and insulin resistance.

The downregulation of HSPs also underscores that angiopathy is likely a feature of cardiac remodeling in T2D. Further implicating perturbed vascular homeostasis, we also found the dysregulation of angiogenesis-related gene programs in ECs, with increased levels of *Pparg* transcripts and other markers of EC dysfunction present. HSP downregulation may also lead to increased rates of vascular cell death and augmented inflammation.[52] Indeed, inflammation in T2D may be exacerbated due to loss of HSP anti-inflammatory activity, which may include direct antagonism of nuclear factor-kappa B (NF-κB) signaling.[53,54] Accordingly, we noted elevated Ly6C^{hi} monocyte levels within the heart and in circulation, as previously reported.[12]

However, our transcriptomic analysis also showed that ligand and receptor genes downregulated in *db/db* hearts were associated with leukocyte trafficking and dampening of inflammation. This was particularly evident within macrophages, fibroblasts, LECs and pericytes. This is in line with recent findings in AngII-induced cardiac fibrosis, where the downregulation of inflammation-related genes occurs in multiple cardiac cell types.[15] We also found that cardiac macrophages increase gene expression of *Ccr2*—encoding the cognate receptor for monocyte chemoattractant protein-1 (MCP-1), a key chemotaxis mediator of monocytes.[55] Cardiac tissue macrophages are inherently anti-inflammatory,[28] therefore augmented expression of *Ccr2* in macrophages may indicate increased immune surveillance and mobilization to inflammatory loci, in attempt to dampen inflammation.

Multiple cell populations also exhibited signs of loss of homeostatic signaling with diabetes. For example, we found increased transcripts corresponding to genes involved in MAPK signaling in ECs, fibroblasts, LECS, macrophages and pericytes, as well as other programs related

to signal transduction. Conversely, cardiac macrophages downregulated genes involved in MAPK signaling. MAPK signaling is directly activated by insulin,[56] hyperglycemia,[57] oxidative stress[58] and other systemic changes induced by diabetes[59] and can drive cellular expansion or death, depending on the activating stressor.[60] Moreover, MAPK signaling is also linked to HSP downregulation; MAPK signaling leads to the phosphorylation of *heat shock factor 1* (HSF1)—the master regulator driving HSP expression—thereby rendering it transcriptionally inactive and thus hindering HSP expression.[61] Our study underscores the importance of cell-specific MAPK dysregulation for diabetes-induced cardiac remodeling.

Consistent with alterations in vascular homeostasis, our analysis also provides insights regarding key lipid modulatory and scavenger molecule genes. Among the top genes upregulated were *Angptl4* and *Ldlr*, which were primarily activated in fibroblasts, as well as *Cd36* in endothelial cells, which has previously been linked to diabetes.[62–64] These molecules are also regulated by MAPK signaling, and have distinct immunomodulatory activities.[65] Indeed, *Cd36* has been linked to promoting inflammation,[66] while increased *Angptl4* expression in mesenchymal cells is considered anti-inflammatory, with mechanisms including the polarization of resident macrophages to an anti-inflammatory phenotype.[67] Additionally, global knockout of the LDL receptor aggravates atherosclerotic plaque burden and foam cell accumulation in mice fed a Western diet,[68] highlighting the importance of LDL-mediated cholesterol efflux in macrophage homeostasis.

Lack of cholesterol transport may also explain the loss of a resident cardiac macrophage subset, characterized by high expression of MHCII. These cells exhibited low transcripts levels for key reverse cholesterol transporter genes *Abca1*, *Cd163*, *Msr1*, *Sra1*, *Tlr4*, and *Apoe*.[69–73] These transporters, in addition to the LDL receptor, collectively govern macrophage viability in hypercholesterolemia[69,74,75]—a major comorbidity in T2D. The impact of losing this macrophage subtype to cardiac homeostasis and pathology remains unclear, however reveals a distinct cellular target for more specific analyses.

Concluding remarks

The findings presented here provide novel insights into the impact of murine T2D on cardiac non-myocytes and the cellular and molecular changes in non-myocytes that may contribute to the pathological remodeling of the heart. This scRNA-seq dataset also offers a useful resource for examining cellular pathways dysregulated by diabetes and provides a critical advancement in knowledge regarding the role of specific cardiac cell types in the phenotype of the diabetic heart. Further, given that these alterations are present where LV diastolic dysfunction is evident, albeit prior to the onset of cardiac fibrosis, suggests that these differences exist as potential drivers of subsequent, clinically significant diabetes-induced adverse cardiac remodeling. Hence, this study provides a critical advancement in knowledge regarding the role of specific cardiac non-myocytes in the phenotype of the diabetic heart, an important step toward better understanding of the causal mechanisms of diabetes-induced cardiomyopathy, and potential insights regarding its optimal management in affected individuals. Future work targeting these pathways may offer new avenues for therapeutics, to address the cardiac complications associated with T2D.

Limitations of the study

Despite providing detailed insights regarding the impact of murine T2D upon cardiac non-myocytes, a number of limitations are worth noting. First, cardiomyocytes were excluded from our analyses, therefore a number of cell specific genes and programs identified here, may extend to myocytes. These may include the activation of genes such as *Pparγ* that we found to be specifically regulated by ECs, while others have also shown to be active in myocytes.[10,76–78] Second, although we have identified changes in MAPK signaling target genes and MAPK signal transduction elements, we have not yet validated these signaling cascades using proteomic means. Third, we did not examine spatial relationships of gene expression patterns. Spatial transcriptomics is an emerging field, allowing for the measurement of spatially resolved transcriptomic information from tissues *in situ*. This however, is also accompanied with its own limitations, with comparatively low cell-specific resolution.[79] Fourth, many gene expression changes in *db/db* mouse hearts may be the product directly related to global leptin receptor deficiency, independent of T2D,[80,81] which has not been explored here. Whilst there are many preclinical models of T2D available, including the milder context imposed by high fat diet in combination with hyperglycemia,[12] the *db/db* model of T2D remains the preferred model of choice for the interrogation of diabetes-induced cardiac abnormalities.[38,82] Finally, our analysis only considered the impact of diabetes in male mice. Cardiac pathology is sex-dependent in mice and humans,[83,84] including in diabetes[18] and we have recently shown cardiac cellular composition, homeostatic cell regulation, and stress responses are dependent upon biological sex.[15,85] We have also shown that female mice with diabetes exhibit a heightened susceptibility to diastolic dysfunction, despite exhibiting a lower extent of hyperglycemia than male mice, with concomitant specific gene expression changes in glucose metabolic and autophagy-related genes.[86] Therefore, whether sex-differences exist in the context of diabetes-induced cardiac remodeling currently remains unknown.

STAR★METHODS

Detailed methods are provided in the online version of this paper and include the following:

- KEY RESOURCES TABLE
- RESOURCE AVAILABILITY
  - Lead contact

SUPPLEMENTAL INFORMATION

Supplemental information can be found online at https://doi.org/10.1016/j.isci.2023.107759.

ACKNOWLEDGMENTS

ARP and RHR received supported from the National Health and Medical Research Council (NHMRC) of Australia, including Ideas Grant GNT1188503 to ARP, Project Grant GNT 1158013 to RHR and MJD, and Senior Research Fellowship GNT1059960 to RHR. CDC, CK and TLG are supported by the La Trobe University Postgraduate Research Scholarship (LTUPRS), Research Training Program Fees Off-set (RTP-Fo) Scholarship. CDC is also supported by a Baker Institute "Bright Sparks" Scholarship and Harold Mitchell Foundation Scholarship. TLG is also supported by a Defence Science Institute RhD Grant. The work was also supported in part by an infrastructure grant from the Victorian Government of Australia.

AUTHOR CONTRIBUTIONS

CDC, MJD, RHR, and ARP conceived the study. RHR, MJD and ARP obtained funding for, and oversaw, the study. CDC and ARP drafted the article. CDC, MJD, MD, and DP performed animal monitoring. CDC and MJD assisted with *in vivo* echocardiography. Echocardiographic imaging was acquired by HK. CDC analyzed echocardiography data. MJD and HK reviewed echocardiography analyses. CDC, MJD, GEF, DP, CK, DMN, ML, TLG, MD, and ARP performed endpoint cull experiments. CDC, IH, MSID, and ARP analyzed *in silico* transcriptomic data. CDC, MJD, GRD, RHR, and ARP regularly reviewed and interpreted the results obtained as they were acquired. All authors read, edited and agreed to submission of the final version of the article.

DECLARATION OF INTERESTS

The authors declare no competing interests.

INCLUSION AND DIVERSITY

We support inclusive, diverse, and equitable conduct of research.

Received: February 21, 2023
Revised: May 1, 2023
Accepted: August 25, 2023
Published: August 28, 2023

REFERENCES

1. Squire, I., Cardoso, J.S., Merkely, B., Martinez, F., Starling, R.C., Desai, A.S., Lefkowitz, M.P., Rizkala, A.R., Rouleau, J.L., Shi, V.C., et al. (2016). Risk Related to Pre – Diabetes Mellitus and Diabetes Mellitus in Heart Failure With Reduced Ejection Fraction Insights From Prospective Comparison of ARNI With ACEI to Determine. Circ Heart Fail *1*, 1–12. https://doi.org/10.1161/CIRCHEARTFAILURE.115.002560.
2. Ritchie, R.H., and Abel, E.D. (2020). Basic mechanisms of diabetic heart disease. Circ. Res. *126*, 1501–1525. https://doi.org/10.1161/CIRCRESAHA.120.315913.
3. Ren, J., and Davidoff, A.J. (1997). Diabetes rapidly induces contractile dysfunctions in isolated ventricular myocytes. Am. J. Physiol. *272*, H148–H158. https://doi.org/10.1152/ajpheart.1997.272.1.H148.
4. Tate, M., Deo, M., Cao, A.H., Hood, S.G., Huynh, K., Kiriazis, H., Du, X.J., Julius, T.L., Figtree, G.A., Dusting, G.J., et al. (2017). Insulin replacement limits progression of diabetic cardiomyopathy in the low-dose streptozotocin-induced diabetic rat. Diabetes Vasc. Dis. Res. *14*, 423–433. https://doi.org/10.1177/1479164117710390.
5. Huynh, K., Bernardo, B.C., McMullen, J.R., and Ritchie, R.H. (2014). Diabetic cardiomyopathy: Mechanisms and new treatment strategies targeting antioxidant signaling pathways. Pharmacol. Ther. *142*, 375–415. https://doi.org/10.1016/j.pharmthera.2014.01.003.
6. Marwick, T.H., Ritchie, R., Shaw, J.E., and Kaye, D. (2018). Implications of Underlying

Mechanisms for the Recognition and Management of Diabetic Cardiomyopathy. J. Am. Coll. Cardiol. *71*, 339–351.

7. Falcão-Pires, I., Hamdani, N., Borbély, A., Gavina, C., Schalkwijk, C.G., van der Velden, J., van Heerebeek, L., Stienen, G.J.M., Niessen, H.W.M., Leite-Moreira, A.F., and Paulus, W.J. (2011). Diabetes mellitus worsens diastolic left ventricular dysfunction in aortic stenosis through altered myocardial structure and cardiomyocyte stiffness. Circulation *124*, 1151–1159. https://doi.org/10.1161/CIRCULATIONAHA.111.025270.
8. Domenighetti, A.A., Danes, V.R., Curl, C.L., Favaloro, J.M., Proietto, J., and Delbridge, L.M.D. (2010). Targeted GLUT-4 deficiency in the heart induces cardiomyocyte hypertrophy and impaired contractility linked with Ca2+ and proton flux dysregulation. J. Mol. Cell. Cardiol. *48*, 663–672. https://doi.org/10.1016/j.yjmcc.2009.11.017.
9. Huynh, K., Kiriazis, H., Du, X.J., Love, J.E., Jandeleit-Dahm, K.A., Forbes, J.M., McMullen, J.R., and Ritchie, R.H. (2012). Coenzyme Q10 attenuates diastolic dysfunction, cardiomyocyte hypertrophy and cardiac fibrosis in the db/db mouse model of type 2 diabetes. Diabetologia *55*, 1544–1553. https://doi.org/10.1007/s00125-012-2495-3.
10. Duan, S.Z., Ivashchenko, C.Y., Russell, M.W., Milstone, D.S., and Mortensen, R.M. (2005). Cardiomyocyte-specfic knockout and agonist of peroxisome proliferator-activated receptor-γ both induce cardiac hypertrophy in mice. Circ. Res. *97*, 372–379. https://doi.org/10.1161/01.RES.0000179226.34112.6d.
11. Phang, R.J., Ritchie, R.H., Hausenloy, D.J., Lees, J.G., and Lim, S.Y. (2023). Cellular interplay between cardiomyocytes and non-myocytes in diabetic cardiomyopathy. Cardiovasc. Res. *119*, 668–690. https://doi.org/10.1093/cvr/cvac049.
12. Cohen, C.D., de Blasio, M.J., Lee, M.K.S., Farrugia, G.E., Prakoso, D., Krstevski, C., Deo, M., Donner, D.G., Kiriazis, H., Flynn, M.C., et al. (2021). Diastolic dysfunction in a pre-clinical model of diabetes is associated with changes in the cardiac non-myocyte cellular composition. Cardiovasc. Diabetol. *20*, 116. https://doi.org/10.1186/s12933-021-01303-9.
13. Pinto, A.R., Ilinykh, A., Ivey, M.J., Kuwabara, J.T., D'Antoni, M.L., Debuque, R., Chandran, A., Wang, L., Arora, K., Rosenthal, N.A., and Tallquist, M.D. (2016). Revisiting cardiac cellular composition. Circ. Res. *118*, 400–409. https://doi.org/10.1161/CIRCRESAHA.115.307778.
14. Skelly, D.A., Squiers, G.T., Mclellan, M.A., Bolisetty, M.T., Robson, P., Rosenthal, N.A., and Pinto, A.R. (2018). Single-cell transcriptional profiling reveals cellular diversity and intercommunication in the mouse heart. Cell Rep. *22*, 600–610. https://doi.org/10.1016/j.celrep.2017.12.072.
15. McLellan, M.A., Skelly, D.A., Dona, M.S.I., Squiers, G.T., Farrugia, G.E., Gaynor, T.L., Cohen, C.D., Pandey, R., Diep, H., Vinh, A., et al. (2020). High-Resolution Transcriptomic Profiling of the Heart during Chronic Stress Reveals Cellular Drivers of Cardiac Fibrosis and Hypertrophy. Circulation *142*, 1448–1463. https://doi.org/10.1161/CIRCULATIONAHA.119.045115.
16. Alexanian, M., Przytycki, P.F., Micheletti, R., Padmanabhan, A., Ye, L., Travers, J.G., Gonzalez-Teran, B., Silva, A.C., Duan, Q., Ranade, S.S., et al. (2021). A transcriptional switch governs fibroblast activation in heart disease. Nature *595*, 438–443. https://doi.org/10.1038/s41586-021-03674-1.
17. Coleman, D.L. (1978). Obese and Diabetes: Two Mutant Genes Causing Diabetes-Obesity Syndromes in Mice. Diabetologia *14*, 141–148.
18. Bowden, M.A., Tesch, G.H., Julius, T.L., Rosli, S., Love, J.E., and Ritchie, R.H. (2015). Earlier onset of diabesity-Induced adverse cardiac remodeling in female compared to male mice. Obesity *23*, 1166–1177. https://doi.org/10.1002/oby.21072.
19. Park, J.-H., and Marwick, T.H. (2011). Use and Limitations of E/e' to Assess Left Ventricular Filling Pressure by Echocardiography. J. Cardiovasc. Ultrasound *19*, 169–173. https://doi.org/10.4250/jcu.2011.19.4.169.
20. Fontes-Carvalho, R., Ladeiras-Lopes, R., Bettencourt, P., Leite-Moreira, A., and Azevedo, A. (2015). Diastolic dysfunction in the diabetic continuum: Association with insulin resistance, metabolic syndrome and type 2 diabetes. Cardiovasc. Diabetol. *14*, 4. https://doi.org/10.1186/s12933-014-0168-x.
21. Kodama, H., Fujita, M., and Yamaguchi, I. (1994). Development of hyperglycaemia and insulin resistance in conscious genetically diabetic (C57BL/KsJ-db/db) mice. Diabetologia *37*, 739–744.
22. Alex, L., Russo, I., Holoborodko, V., and Frangogiannis, N.G. (2018). Characterization of a mouse model of obesity-related fibrotic cardiomyopathy that recapitulates features of human heart failure with preserved ejection fraction. Am. J. Physiol. Heart Circ. Physiol. *315*, H934–H949. https://doi.org/10.1152/ajpheart.00238.2018.-Heart.
23. Daniels, A., van Bilsen, M., Janssen, B.J.A., Brouns, A.E., Cleutjens, J.P.M., Roemen, T.H.M., Schaart, G., van der Velden, J., van der Vusse, G.J., and van Nieuwenhoven, F.A. (2010). Impaired cardiac functional reserve in type 2 diabetic db/db mice is associated with metabolic, but not structural, remodelling. Acta Physiol. *200*, 11–22. https://doi.org/10.1111/j.1748-1716.2010.02102.x.
24. Köster, A., Chao, Y.B., Mosior, M., Ford, A., Gonzalez-DeWhitt, P.A., Hale, J.E., Li, D., Qiu, Y., Fraser, C.C., Yang, D.D., et al. (2005). Transgenic angiopoietin-like (Angptl)4 overexpression and targeted disruption of Angptl4 and Angptl3: Regulation of triglyceride metabolism. Endocrinology *146*, 4943–4950. https://doi.org/10.1210/en.2005-0476.
25. Lehrke, M., and Lazar, M.A. (2005). The many faces of PPARγ. Cell *123*, 993–999. https://doi.org/10.1016/j.cell.2005.11.026.
26. Dulyaninova, N.G., Ruiz, P.D., Gamble, M.J., Backer, J.M., and Bresnick, A.R. (2018). S100A4 regulates macrophage invasion by distinct myosin-dependent and myosin-independent mechanisms. Mol. Biol. Cell *29*, 632–642. https://doi.org/10.1091/mbc.E17-07-0460.
27. Leclerc, E., Fritz, G., Weibel, M., Heizmann, C.W., and Galichet, A. (2007). S100B and S100A6 differentially modulate cell survival by interacting with distinct RAGE (receptor for advanced glycation end products) immunoglobulin domains. J. Biol. Chem. *282*, 31317–31331. https://doi.org/10.1074/jbc.M703951200.
28. Pinto, A.R., Paolicelli, R., Salimova, E., Gospocic, J., Slonimsky, E., Bilbao-Cortes, D., Godwin, J.W., and Rosenthal, N.A. (2012). An abundant tissue macrophage population in the adult murine heart with a distinct alternatively-activated macrophage profile. PLoS One *7*, e36814. https://doi.org/10.1371/journal.pone.0036814.
29. Boulton, A.J.M., Malik, R.A., Arezzo, J.C., and Sosenko, J.M. (2004). Diabetic Somatic Neuropathies. Diabetes Care. https://doi.org/10.2337/diacare.27.6.1458.
30. Basu, S., Vadaie, N., Prabhakar, A., Li, B., Adhikari, H., Pitoniak, A., Chow, J., Chavel, C.A., and Cullen, P.J. (2016). Spatial landmarks regulate a Cdc42-dependent MAPK pathway to control differentiation and the response to positional compromise. Proc Natl Acad Sci USA *113*, E2019–E2028. https://doi.org/10.1073/pnas.1522679113.
31. Efremova, M., Vento-Tormo, M., Teichmann, S.A., and Vento-Tormo, R. (2020). CellPhoneDB: inferring cell–cell communication from combined expression of multi-subunit ligand–receptor complexes. Nat. Protoc. *15*, 1484–1506. https://doi.org/10.1038/s41596-020-0292-x.
32. de Luna, N., Gallardo, E., Sonnet, C., Chazaud, B., Dominguez-Perles, R., Suarez-Calvet, X., Gherardi, R.K., and Illa, I. (2010). Role of Thrombospondin 1 in Macrophage Inflammation in Dysferlin Myopathy.
33. Guerrero-Esteo, M., Lastres, P., Letamendia, A., Perez-Alvarez, M.J., Langa, C., López, L.A., Fabra, A., Garcia-Pardo, A., Vera, S., Letarte, M., et al. (1999). Endoglin Overexpression Modulates Cellular Morphology, Migration, and Adhesion of Mouse Fibroblasts.
34. Sun, P.H., Ye, L., Mason, M.D., and Jiang, W.G. (2012). Protein Tyrosine Phosphatase μ (PTP μ or PTPRM), a Negative Regulator of Proliferation and Invasion of Breast Cancer Cells, Is Associated with Disease Prognosis. PLoS One *7*, e50183. https://doi.org/10.1371/journal.pone.0050183.
35. de Bruyn, M., Wiersma, V.R., Helfrich, W., Eggleton, P., and Bremer, E. (2015). The ever-expanding immunomodulatory role of calreticulin in cancer immunity. Front. Oncol. *5*, 35. https://doi.org/10.3389/fonc.2015.00035.
36. Krstevski, C., Cohen, C.D., Dona, M.S.I., and Pinto, A.R. (2020). New perspectives of the cardiac cellular landscape: mapping cellular mediators of cardiac fibrosis using single-cell transcriptomics. Biochem. Soc. Trans. *48*, 2483–2493. https://doi.org/10.1042/bst20191255.
37. Mathews, C.E., Langley, S.H., and Leiter, E.H. (2002). New Mouse Model To Study Islet Transplantation In Insulin-Dependent Diabetes Mellitus. Transplantation *73*, 1333–1336.
38. Prakoso, D., de Blasio, M.J., Tate, M., and Ritchie, R.H. (2022). Current landscape of preclinical models of diabetic cardiomyopathy. Trends Pharmacol. Sci. *43*, 940–956. https://doi.org/10.1016/j.tips.2022.04.005.
39. Hamdani, N., Hervent, A.S., Vandekerckhove, L., Matheeussen, V., Demolder, M., Baerts, L., de Meester, I., Linke, W.A., Paulus, W.J., and de Keulenaer, G.W. (2014). Left ventricular diastolic dysfunction and myocardial stiffness in diabetic mice is attenuated by inhibition of dipeptidyl peptidase 4. Cardiovasc. Res. *104*, 423–431. https://doi.org/10.1093/cvr/cvu223.
40. Wang, S., Wang, C., Turdi, S., Richmond, K.L., Zhang, Y., and Ren, J. (2018). ALDH2 protects against high fat diet-induced obesity cardiomyopathy and defective autophagy: Role of CaM kinase II, histone H3K9 methyltransferase SUV39H, Sirt1, and PGC-1α deacetylation. Int. J. Obes. *42*, 1073–1087. https://doi.org/10.1038/s41366-018-0030-4.

41. Miranda-Silva, D., Wüst, R.C.I., Conceição, G., Gonçalves-Rodrigues, P., Gonçalves, N., Gonçalves, A., Kuster, D.W.D., Leite-Moreira, A.F., van der Velden, J., de Sousa Beleza, J.M., et al. (2020). Disturbed cardiac mitochondrial and cytosolic calcium handling in a metabolic risk-related rat model of heart failure with preserved ejection fraction. Acta Physiol. *228*, e13378. https://doi.org/10.1111/apha.13378.
42. Kesherwani, V., Shahshahan, H.R., and Mishra, P.K. (2017). Cardiac transcriptome profiling of diabetic Akita mice using microarray and next generation sequencing. PLoS One *12*, e0182828. https://doi.org/10.1371/journal.pone.0182828.
43. Wilson, K.D., Li, Z., Wagner, R., Yue, P., Tsao, P., Nestorova, G., Huang, M., Hirschberg, D.L., Yock, P.G., Quertermous, T., and Wu, J.C. (2008). Transcriptome alteration in the diabetic heart by rosiglitazone: Implications for cardiovascular mortality. PLoS One *3*, e2609. https://doi.org/10.1371/journal.pone.0002609.
44. Khassaf, M., McArdle, A., Esanu, C., Vasilaki, A., McArdle, F., Griffiths, R.D., Brodie, D.A., and Jackson, M.J. (2003). Effect of vitamin C supplements on antioxidant defence and stress proteins in human lymphocytes and skeletal muscle. J. Physiol. *549*, 645–652. https://doi.org/10.1113/jphysiol.2003.040303.
45. Lindquist, S., and Craig, E.A. (1988). The heat shock proteins. Annu. Rev. Genet. *22*, 631–677.
46. Westerheide, S.D., Kawahara, T.L.A., Orton, K., and Morimoto, R.I. (2006). Triptolide, an inhibitor of the human heat shock response that enhances stress-induced cell death. J. Biol. Chem. *281*, 9616–9622. https://doi.org/10.1074/jbc.M512044200.
47. Chung, J., Nguyen, A.K., Henstridge, D.C., Holmes, A.G., Chan, M.H.S., Mesa, J.L., Lancaster, G.I., Southgate, R.J., Bruce, C.R., Duffy, S.J., et al. (2008). HSP72 protects against obesity-induced insulin resistance *105*, 1739–1744. https://doi.org/10.1073/pnas.0705799105.
48. Lazaro, I., Oguiza, A., Recio, C., Mallavia, B., Madrigal-Matute, J., Blanco, J., Egido, J., Martin-Ventura, J.L., and Gomez-Guerrero, C. (2015). Targeting HSP90 ameliorates nephropathy and atherosclerosis through suppression of NF-κB and STAT signaling pathways in diabetic mice. Diabetes *64*, 3600–3613. https://doi.org/10.2337/db14-1926.
49. Febbraio, M.A., and Koukoulas, I. (2000). HSP72 gene expression progressively increases in human skeletal muscle during prolonged, exhaustive exercise. J. Appl. Physiol. *89*, 1055–1060.
50. Henstridge, D.C., Bruce, C.R., Drew, B.G., Tory, K., Kolonics, A., Estevez, E., Chung, J., Watson, N., Gardner, T., Lee-Young, R.S., et al. (2014). Activating HSP72 in rodent skeletal muscle increases mitochondrial number and oxidative capacity and decreases insulin resistance. Diabetes *63*, 1881–1894. https://doi.org/10.2337/db13-0967.
51. Salo, D.C., Donovan, C.M., and Davies, K.J. (1991). HSP70 and other possible heat shock or oxidative stress proteins are induced in skeletal muscle, heart, and liver during exercise. Free Radic. Biol. Med. *11*, 239–246.
52. Sprague, A.H., and Khalil, R.A. (2009). Inflammatory cytokines in vascular dysfunction and vascular disease. Biochem. Pharmacol. *78*, 539–552. https://doi.org/10.1016/j.bcp.2009.04.029.
53. Wang, C.H., Chou, P.C., Chung, F.T., Lin, H.C., Huang, K.H., and Kuo, H.P. (2017). Heat shock protein70 is implicated in modulating NF-κ B activation in alveolar macrophages of patients with active pulmonary tuberculosis. Sci. Rep. *7*, 1214. https://doi.org/10.1038/s41598-017-01405-z.
54. Wang, Y., Liu, J., Kong, Q., Cheng, H., Tu, F., Yu, P., Liu, Y., Zhang, X., Li, C., Li, Y., et al. (2019). Cardiomyocyte-specific deficiency of HSPB1 worsens cardiac dysfunction by activating NFκB-mediated leucocyte recruitment after myocardial infarction. Cardiovasc. Res. *115*, 154–167. https://doi.org/10.1093/cvr/cvy163.
55. Gregory, J.L., Morand, E.F., McKeown, S.J., Ralph, J.A., Hall, P., Yang, Y.H., McColl, S.R., and Hickey, M.J. (2006). Macrophage Migration Inhibitory Factor Induces Macrophage Recruitment via CC Chemokine Ligand 2. J. Immunol. *177*, 8072–8079. https://doi.org/10.4049/jimmunol.177.11.8072.
56. Kim, Y.-B., Uotani, S., Pierroz, D.D., Flier, J.S., and Kahn, B.B. (2000). *In Vivo* Administration of Leptin Activates Signal Transduction Directly in Insulin-Sensitive Tissues: Overlapping but Distinct Pathways from Insulin. Endocrinology *141*, 2328–2339.
57. Schiekofer, S., Andrassy, M., Chen, J., Rudofsky, G., Schneider, J., Wendt, T., Stefan, N., Humpert, P., Fritsche, A., Stumvoll, M., et al. (2003). Acute Hyperglycemia Causes Intracellular Formation of CML and Activation of ras, p42/44 MAPK, and Nuclear Factor B in PBMCs. Diabetes *52*, 621–633.
58. Huang, A., Yang, Y.M., Yan, C., Kaley, G., Hintze, T.H., and Sun, D. (2012). Altered MAPK signaling in progressive deterioration of endothelial function in diabetic mice. Diabetes *61*, 3181–3188. https://doi.org/10.2337/db12-0559.
59. Hsueh, W.A., and Law, R.E. (1999). Insulin Signaling in the Arterial Wall. Am. J. Cardiol. *84*, 21–24.
60. Plotnikov, A., Zehorai, E., Procaccia, S., and Seger, R. (2011). The MAPK cascades: Signaling components, nuclear roles and mechanisms of nuclear translocation. Biochim. Biophys. Acta *1813*, 1619–1633. https://doi.org/10.1016/j.bbamcr.2010.12.012.
61. Chu, B., Zhong, R., Soncin, F., Stevenson, M.A., and Calderwood, S.K. (1998). Transcriptional activity of heat shock factor 1 at 37 °c is repressed through phosphorylation on two distinct serine residues by glycogen synthase kinase 3α and protein kinases cα and cζ. J. Biol. Chem. *273*, 18640–18646. https://doi.org/10.1074/jbc.273.29.18640.
62. Gusarova, V., O'Dushlaine, C., Teslovich, T.M., Benotti, P.N., Mirshahi, T., Gottesman, O., van Hout, C.v., Murray, M.F., Mahajan, A., Nielsen, J.B., et al. (2018). Genetic inactivation of ANGPTL4 improves glucose homeostasis and is associated with reduced risk of diabetes. Nat. Commun. *9*, 2252. https://doi.org/10.1038/s41467-018-04611-z.
63. Edgar, L., Akbar, N., Braithwaite, A.T., Krausgruber, T., Gallart-Ayala, H., Bailey, J., Corbin, A.L., Khoyratty, T.E., Chai, J.T., Alkhalil, M., et al. (2021). Hyperglycemia Induces Trained Immunity in Macrophages and Their Precursors and Promotes Atherosclerosis. Circulation *144*, 961–982. https://doi.org/10.1161/CIRCULATIONAHA.120.046464.
64. Mansor, L.S., Sousa Fialho, M.d.L., Yea, G., Coumans, W.A., West, J.A., Kerr, M., Carr, C.A., Luiken, J.J.F.P., Glatz, J.F.C., Evans, R.D., et al. (2017). Inhibition of sarcolemmal FAT/CD36 by sulfo-N-succinimidyl oleate rapidly corrects metabolism and restores function in the diabetic heart following hypoxia/reoxygenation. Cardiovasc. Res. *113*, 737–748. https://doi.org/10.1093/cvr/cvx045.
65. Bujold, K., Rhainds, D., Jossart, C., Febbraio, M., Marleau, S., and Ong, H. (2009). CD36-mediated cholesterol efflux is associated with PPARγ activation via a MAPK-dependent COX-2 pathway in macrophages. Cardiovasc. Res. *83*, 457–464. https://doi.org/10.1093/cvr/cvp118.
66. Kennedy, D.J., Kuchibhotla, S., Westfall, K.M., Silverstein, R.L., Morton, R.E., and Febbraio, M. (2011). A CD36-dependent pathway enhances macrophage and adipose tissue inflammation and impairs insulin signalling. Cardiovasc. Res. *89*, 604–613. https://doi.org/10.1093/cvr/cvq360.
67. Cho, D.I., Kang, H.J., Jeon, J.H., Eom, G.H., Cho, H.H., Kim, M.R., Cho, M., Jeong, H.Y., Cho, H.C., Hong, M.H., et al. (2019). Antiinflammatory activity of ANGPTL4 facilitates macrophage polarization to induce cardiac repair. JCI Insight *4*, e125437. https://doi.org/10.1172/jci.insight.125437.
68. Kusters, D.H.M., Chatrou, M.L., Willems, B.A.G., de Saint-Hubert, M., Bauwens, M., van der Vorst, E., Bena, S., Biessen, E.A.L., Perretti, M., Schurgers, L.J., and Reutelingsperger, C.P.M. (2015). Pharmacological treatment with annexin A1 reduces atherosclerotic plaque burden in LDLR-/- mice on Western Type Diet. PLoS One *10*, e0130484. https://doi.org/10.1371/journal.pone.0130484.
69. Zanotti, I., Pedrelli, M., Potì, F., Stomeo, G., Gomaraschi, M., Calabresi, L., and Bernini, F. (2011). Macrophage, but not systemic, apolipoprotein e is necessary for macrophage reverse cholesterol transport *in vivo*. Arterioscler. Thromb. Vasc. Biol. *31*, 74–80. https://doi.org/10.1161/ATVBAHA.110.213892.
70. Azzam, K.M., and Fessler, M.B. (2012). Crosstalk between reverse cholesterol transport and innate immunity. Trends Endocrinol. Metabol. *23*, 169–178. https://doi.org/10.1016/j.tem.2012.02.001.
71. Attie, A.D., Kastelein, J.P., and Hayden, M.R. (2001). Pivotal role of ABCA1 in reverse cholesterol transport influencing HLD levels and susceptibility to atherosclerosis. J. Lipid Res. *42*, 1717–1726. https://doi.org/10.1016/s0022-2275(20)31498-x.
72. Bengtsson, E., Hultman, K., Edsfeldt, A., Persson, A., Nitulescu, M., Nilsson, J., Gonçalves, I., and Björkbacka, H. (2020). CD163+ macrophages are associated with a vulnerable plaque phenotype in human carotid plaques. Sci. Rep. *10*, 14362. https://doi.org/10.1038/s41598-020-71110-x.
73. Haasken, S., Auger, J.L., Taylor, J.J., Hobday, P.M., Goudy, B.D., Titcombe, P.J., Mueller, D.L., and Binstadt, B.A. (2013). Macrophage Scavenger Receptor 1 (Msr1, SR-A) Influences B Cell Autoimmunity by Regulating Soluble Autoantigen Concentration. J. Immunol. *191*, 1055–1062. https://doi.org/10.4049/jimmunol.1201680.
74. Wang, X., Collins, H.L., Ranalletta, M., Fuki, I.v., Billheimer, J.T., Rothblat, G.H., Tall, A.R., and Rader, D.J. (2007). Macrophage ABCA1 and ABCG1, but not SR-BI, promote

macrophage reverse cholesterol transport *in vivo*. J. Clin. Invest. *117*, 2216–2224. https://doi.org/10.1172/JCI32057.

75. Mauldin, J.P., Srinivasan, S., Mulya, A., Gebre, A., Parks, J.S., Daugherty, A., and Hedrick, C.C. (2006). Reduction in ABCG1 in type 2 diabetic mice increases macrophage foam cell formation. J. Biol. Chem. *281*, 21216–21224. https://doi.org/10.1074/jbc.M510952200.
76. Son, N.H., Park, T.S., Yamashita, H., Yokoyama, M., Huggins, L.A., Okajima, K., Homma, S., Szabolcs, M.J., Huang, L.S., and Goldberg, I.J. (2007). Cardiomyocyte expression of PPARγ leads to cardiac dysfunction in mice. J. Clin. Invest. *117*, 2791–2801. https://doi.org/10.1172/JCI30335.
77. Nagendran, J., Pulinilkunnil, T., Kienesberger, P.C., Sung, M.M., Fung, D., Febbraio, M., and Dyck, J.R.B. (2013). Cardiomyocyte-specific ablation of CD36 improves post-ischemic functional recovery. J. Mol. Cell. Cardiol. *63*, 180–188. https://doi.org/10.1016/j.yjmcc.2013.07.020.
78. Costantino, S., Akhmedov, A., Melina, G., Mohammed, S.A., Othman, A., Ambrosini, S., Wijnen, W.J., Sada, L., Ciavarella, G.M., Liberale, L., et al. (2019). Obesity-induced activation of JunD promotes myocardial lipid accumulation and metabolic cardiomyopathy. Eur. Heart J. *40*, 997–1008. https://doi.org/10.1093/eurheartj/ehy903.
79. Larsson, L., Frisén, J., and Lundeberg, J. (2021). Spatially resolved transcriptomics adds a new dimension to genomics. Nat. Methods *18*, 15–18. https://doi.org/10.1038/s41592-020-01038-7.
80. Barouch, L.A., Berkowitz, D.E., Harrison, R.W., O'Donnell, C.P., and Hare, J.M. (2003). Disruption of leptin signaling contributes to cardiac hypertrophy independently of body weight in mice. Circulation *108*, 754–759. https://doi.org/10.1161/01.CIR.0000083716.82622.FD.
81. McGaffin, K.R., Witham, W.G., Yester, K.A., Romano, L.C., Odoherty, R.M., McTiernan, C.F., and Odonnell, C.P. (2011). Cardiac-specific leptin receptor deletion exacerbates ischaemic heart failure in mice. Cardiovasc. Res. *89*, 60–71. https://doi.org/10.1093/cvr/cvq288.
82. Heather, L.C., Hafstad, A.D., Halade, G. v, Harmancey, R., Mellor, K.M., Mishra, P.K., Mulvihill, E.E., Nabben, M., Nakamura, M., Rider, O.J., et al. (2022). Guidelines on Models of Diabetic Heart Disease. Am. J. Physiol. Heart Circ. Physiol. *323*, H176–H200. https://doi.org/10.1152/ajpheart.00058.2022.
83. Beale, A.L., Meyer, P., Marwick, T.H., Lam, C.S.P., and Kaye, D.M. (2018). Sex differences in cardiovascular pathophysiology why women are overrepresented in heart failure with preserved ejection fraction. Circulation *138*, 198–205. https://doi.org/10.1161/CIRCULATIONAHA.118.034271.
84. Kessler, E.L., Rivaud, M.R., Vos, M.A., and van Veen, T.A.B. (2019). Sex-specific influence on cardiac structural remodeling and therapy in cardiovascular disease. Biol. Sex Differ. *10*, 7. https://doi.org/10.1186/s13293-019-0223-0.
85. Squiers, G.T., Mclellan, M.A., Ilinykh, A., Branca, J., Rosenthal, N.A., and Pinto, A.R. (2020). Cardiac cellularity is dependent upon biological sex and is regulated by gonadal hormones. Cardiovasc. Res. *117*, 2252–2262. https://doi.org/10.1093/cvr/cvaa265/5907911.
86. Chandramouli, C., Reichelt, M.E., Curl, C.L., Varma, U., Bienvenu, L.A., Koutsifeli, P., Raaijmakers, A.J.A., de Blasio, M.J., Qin, C.X., Jenkins, A.J., et al. (2018). Diastolic dysfunction is more apparent in STZ-induced diabetic female mice, despite less pronounced hyperglycemia. Sci. Rep. *8*, 2346. https://doi.org/10.1038/s41598-018-20703-8.
87. Mehlem, A., Hagberg, C.E., Muhl, L., Eriksson, U., and Falkevall, A. (2013). Imaging of neutral lipids by oil red O for analyzing the metabolic status in health and disease. Nat. Protoc. *8*, 1149–1154. https://doi.org/10.1038/nprot.2013.055.
88. Pinto, A.R., Chandran, A., Rosenthal, N.A., and Godwin, J.W. (2013). Isolation and analysis of single cells from the mouse heart. J. Immunol. Methods *393*, 74–80. https://doi.org/10.1016/j.jim.2013.03.012.
89. Farrugia, G.E., McLellan, M.A., Weeks, K.L., Matsumoto, A., Cohen, C.D., Krstevski, C., Gaynor, T.L., Parslow, A.C., McMullen, J.R., and Pinto, A.R. (2021). A protocol for rapid and parallel isolation of myocytes and non-myocytes from multiple mouse hearts. STAR Protoc. *2*, 100866–100917. https://doi.org/10.1016/j.xpro.2021.100866.
90. Ackers-Johnson, M., Li, P.Y., Holmes, A.P., O'Brien, S.M., Pavlovic, D., and Foo, R.S. (2016). A simplified, langendorff-free method for concomitant isolation of viable cardiac myocytes and nonmyocytes from the adult mouse heart. Circ. Res. *119*, 909–920. https://doi.org/10.1161/CIRCRESAHA.116.309202.
91. Finak, G., McDavid, A., Yajima, M., Deng, J., Gersuk, V., Shalek, A.K., Slichter, C.K., Miller, H.W., McElrath, M.J., Prlic, M., et al. (2015). MAST: A flexible statistical framework for assessing transcriptional changes and characterizing heterogeneity in single-cell RNA sequencing data. Genome Biol. *16*, 278. https://doi.org/10.1186/s13059-015-0844-5.
92. Soneson, C., and Robinson, M.D. (2018). Bias, robustness and scalability in single-cell differential expression analysis. Nat. Methods *15*, 255–261. https://doi.org/10.1038/nmeth.4612.
93. Yu, G., Wang, L.G., Han, Y., and He, Q.Y. (2012). ClusterProfiler: An R package for comparing biological themes among gene clusters. OMICS *16*, 284–287. https://doi.org/10.1089/omi.2011.0118.

STAR★METHODS

KEY RESOURCES TABLE

REAGENT or RESOURCE	SOURCE	IDENTIFIER
Antibodies		
DAPI	Sigma-Aldrich	D9542-5MG
CD45R/B220	BD Biosciences	103241 RA3-6B2
CD3ϵ	BD Biosciences	11-0033-81 500A2
Gr1 (Ly6G/Ly6C)	BD Biosciences	552093 RB6-8C5
CD115	BD Biosciences	135506 AFS98
CD4	BD Biosciences	116016 RM4-4
CD8	BD Biosciences	126612 YTS156.7.7
CD45	BD Biosciences	557659 30-F11
CD31	BD Biosciences	740879 390
I-A/I-E (MHCII)	BD Biosciences	743876 2G9
CD11b	BD Biosciences	564443 M1/70
CD64 (a & b allo-antigens)	BD Biosciences	740622 X54-5/7.1
CD146 (Mcam)	BD Biosciences	740827 ME-9F1
eBioscience™ Calcein Blue AM Viability Dye	Invitrogen	65-0855-39
Ly6G	Biolegend	127648 1A8
NK1.1	Biolegend	108716 PK136
CD59a	Miltenyi Biotec	130-104-105 REA287
CD39	Biolegend	143806 Duha59
SYTOX™ Green Dead Cell Stain	Invitrogen	S34860
CD90.2	Invitrogen	105320 30-H12
Ly6C	Biolegend	128012 HK1.4
Chemicals, peptides, and recombinant proteins		
Oil-red O stain	Sigma Aldrich	ORO [C26H24N4O]
Collagenase type IV	Worthington Biochemical Corporation	CLS-4
Dispase II	Roche	04942078001
Lysis buffer for red blood cells	Becton Dickinson, USA	555899
Critical commercial assays		
Blood glucose measured by glucometer	Roche Diagnostics	Accu-Chek® Performa II
HbA1c	Roche Diagnostics	Cobas b 101 POC system
Deposited data		
Sequencing data is publicly available	Array Express	Accession number E-MTAB-11940
Experimental models: Organisms/strains		
[B6.BKS(D)-Lepr^{db}/J] (*db/db*) and heterozygous non-diabetic, age-matched littermate controls (*db/h*)	The Jackson Laboratory (Bar Harbor ME, USA).	Stock identifier: #000697
Software and algorithms		
CellPhoneDb	https://www.cellphonedb.org/	Version 2.1.7
Cell Ranger software version 5.0.0	10X Genomics	Version 5
R studio	https://www.posit.co/products/open-source/rstudio	Version 4.1
Seurat suite	https://satijalab.org/seurat/	Version 3.2.0

(*Continued on next page*)

Continued

REAGENT or RESOURCE	SOURCE	IDENTIFIER
R packages, RVenn (v1.10), Euller (v6.10), VennDiagram (v1.6.20) and Venneuler (v1.1-0)	https://CRAN.R-project.org/package=RVenn https://CRAN.R-project.org/package=eulerr https://CRAN.R-project.org/package=VennDiagram https://CRAN.R-project.org/package=venneuler	As noted with package name.
EnrichGO function within the 'clusterProfiler' R package	https://doi.org/10.18129/B9.bioc.clusterProfiler	Version 3.12.0
BioMart database accessed using the biomaRt R package	https://doi.org/10.18129/B9.bioc.biomaRt	v100
Circlize R package	https://cran.r-project.org/web/packages/circlize/index.html	V0.4.15
Other		
Cardiac bulk RNA-seq datasets from 12 week-old 'Akita' (Ins2 Akita mice (Gene Expression Omnibus accession number GSE66577) and 13 week-old db/db mice (GSE36875).	Gene Expression Omnibus (GEO)	GSE66577, GSE36875
EchoMRI	EchoMRI, Houston, TX, USA	Echo-MRI™ 4-in-1 700 Analyser
Echocardiography	Philips	iE33 ultrasound machine
Bright field scanning microscope	Monash University Histology Platform	Aperio Scanscope AT Turbo
LSR Fortessa™ X-20 Special Order flow cytometer	Becton Dickinson, USA	X-20 Special Order
FACS Aria™ Fusion Flow Cytometer for fluorescence-activated cell sorting (FACS)	Becton Dickinson, USA	Aria™ Fusion
Single cell library preparation using a 10X Chromium controller	10X Genomics	Chromium X Series
Sequencing was performed on an Illumina NovaSeq 6000 system	Illumina	NovaSeq 6000

RESOURCE AVAILABILITY

Lead contact

Any further information and requests for resources should be directed to, and will be fulfilled by the Lead Contact, Alex Pinto (alex.pinto@baker.edu.au).

Materials availability

This study did not produce any new or unique reagents.

Data and code availability

Sequencing data relating to this study is publicly available at Array Express, accession number E-MTAB-11940. All scripts and metadata related to this paper are available at https://github.com/pinto-lab/Cohen-et-al-2023_dbdb_nonmyocytes.

EXPERIMENTAL MODEL AND STUDY PARTICIPANT DETAILS

Lep*db* (*db/db*, stock #000697) male mice were purchased from The Jackson Laboratory (Bar Harbor ME, USA) and monitored until mice reached both 10 and 17-weeks of age. All animal-related experiments were approved by the Alfred Research Alliance (ARA) Animal Ethics Committee (Ethics number: E/1880/2019/B) and were performed in accordance with the National Health and Medical Research Council of Australia guidelines.

METHOD DETAILS

Murine physiological analyses

In order to assess severity of diabetes, we conducted a range of physiological assessments. Mice had free access to food and water and were housed at 22°C on a 12 h light/dark cycle. Blood glucose measurements were performed bi-monthly, using a glucometer (Accu-Chek® Performa II, Roche Diagnostics). Body weight (g) was also measured fortnightly. Percentage glycated haemoglobin (% HbA1c) was also measured at endpoint to assess long-term blood glucose handling (Cobas b 101 POC system, Roche Diagnostics). Whole-body composition analysis was performed at endpoint using an Echo-MRI™ 4-in-1 700 Analyser (EchoMRI, Houston, TX, USA), to determine any differences in fat and lean mass.

Endpoint echocardiography was also performed to assess cardiac function *in vivo*. Echocardiography was conducted in mice under anaesthesia (Ketamine/Xylazine/Atropine [KXA], 80/8/0.96mg/kg, i.p.) at endpoint, with assistance from the Baker Heart and Diabetes Institute Preclinical Cardiology Microsurgery & Imaging Platform (PCMIP). Before image acquisition, mice were anaesthetised and their thoracic area was shaved, after which ultrasound transmission gel was added to assist in optimal visualisation of raw echocardiography data. A Philips iE33 ultrasound machine with a 15-MHz linear-array and 12-MHz sector transducer (North Ryde, Australia) was used for all animals to assess the degree of cardiac functional impairment *in vivo*.

Doppler flow echocardiography was used to assess cardiac transmitral flow velocity in each phase of diastole. The early phase (E wave) and the late atrial phase (A wave) of diastole were measured to determine the E:A ratio - an established measurement of LV diastolic function (Figure S2B). Other measurements of diastole were also measured including deceleration time (DT), isovolumic relaxation time (IVRT) and heart rate (HR; anaesthetised HR, Figure 2B). In a similar manner, tissue Doppler echocardiography was performed to examine the tissue motion of the mitral annulus. Peak mitral velocities were obtained from raw echocardiography traces (Figure S2C) and measured as indicated in Figure S2D (early phase: e'; late atrial phase: a' wave). The e':a' and E/e' ratios were calculated and used as additional measures to assess diastolic function.

M-Mode echocardiography was used to measure any alterations in wall thicknesses between experimental mouse cohorts, and to determine any aberrances in systolic function (Figures S2E and S2F). M-mode derived measurements include; anterior (AWd) and posterior (PWd) wall thicknesses, left ventricular end-diastolic dimension (LVEDD), left ventricular end-systolic dimension (LVESD). Fractional shortening (FS) was also calculated (%FS = 100 × [LVEDD-LVESD] / LVEDD) as an index of LV systolic function.

Histology

A separate age-matched cohort of *db/db* and *db/h* mice at 17 weeks of age were utilized for basic cardiac histology, embedded into Optimal Cutting Temperature (OCT) compound and stored at -80°C. Immunohistochemistry (IHC) staining on formalin-fixed paraffin-embedded (FFPE) tissue was performed on hearts obtained from 20-week-old *db/db* and *db/h* mice. For all histology, the mid-portion of the left ventricle (LV), right ventricle (RV), and intra-ventricular septum (IVS) was sliced into approximately 1 mm thick sections prior to embedding. Subsequently, cardiac cross-sections were cut at a thickness of 10μm for OCT samples, and 4μm for FFPE embedded samples.

Oil-red O staining (ORO [$C_{26}H_{24}N_4O$], Sigma Aldrich) was used to assess the content of neutral cardiac lipids, as described.[87] Picro-sirius red staining was also performed by the Monash University Histology Platform to determine the degree of cardiac ECM deposition. Brightfield micrographs were acquired by the Monash University Histology Platform (VIC, Australia), using a bright field scanning microscope (Aperio Scanscope AT Turbo, Monash Histology Platform) for analysis. Histological micrographs were subsequently analysed using Fiji software for quantification of lipid droplets and cardiac fibrosis, respectively.

Cardiac single-cell isolation and flow cytometry

For cardiac flow cytometry experiments, the thoracic cavity was exposed and right atria was cut to allow for cardiac perfusion (perfusate contained cold PBS supplemented with 0.9mM $CaCl_2$, 200mM KCl) through the LV as described previously.[88] Hearts were perfused via 30G hypodermic needles attached to a peristaltic pump at a rate of 4mL/min (Cole Palmer, IL, USA) for ~15 minutes or until the blood within the liver had cleared. Following perfusion, cardiac ventricles (right & left ventricle, intra-ventricular septum) were isolated and placed in 5mL Eppendorf™ tubes with 3mL of 'enzymatic digestion buffer' (2mg/mL collagenase type IV [CLS-4, Worthington Biochemical Corporation], 1.2U/mL Dispase II [04942078001, Roche] in PBS supplemented with 0.9mM/L $CaCl_2$). To facilitate digestion, the tissue and *enzymatic digestion buffer* were incubated at 37°C for 45 minutes and triturated at 15-minute intervals during incubation. Next, cell suspensions from each sample were individually filtered through a 70μM cell strainer into a 15mL tube containing 10mL of PBS (supplemented with 0.9mM/L $CaCl_2$). Samples were then centrifuged at 200×g for 15-minutes at 4°C with centrifuge brakes deactivated, for debris clearance. The supernatant was aspirated and cell pellets were resuspended in 200μl of 2% FCS/HBSS buffer, before staining with a specific antibody panel for flow cytometry (Figure S3). Cardiac non-myocyte cells were filtered through 35μM mesh into 5mL polystyrene round-bottom tubes (352052, Falcon®, NY, USA) and identified using the specific antibody panel on a BD LSR Fortessa™ X-20 Special Order flow cytometer.

Whole blood was obtained by cardiac puncture at endpoint and stained using a leukocyte-specific antibody panel. Blood was then subjected to red blood cell (RBC) lysis for 15 minutes at 4°C using an ammonium chloride based commercial lysis buffer (1X dilution, 555899, Becton Dickinson, USA). After RBC lysis, the remaining stained cells were washed twice in 2% FCS/HBSS. Between each wash, cells were centrifuged at 400×g for 5 minutes at 4°C. Cells were then resuspended in 200μl of 2% FCS/HBSS buffer containing DAPI (0.1μg/mL); and

filtered through 35μM mesh into 5mL polystyrene round-bottom tubes (352052, Falcon®, NY, USA) for flow cytometry, using the aforementioned cytometer.

Single-cell RNA sequencing

For single-cell RNA sequencing (scRNAseq) cardiac single cell suspensions were prepared following a modified Langendorff approach described previously.[89] Briefly, after euthanasia, the thoracic cavity was opened and the inferior *vena cava* was ligated, before injecting 7mL of cold 'EDTA buffer'[89,90] into the right ventricle for perfusion. Following perfusion, hearts were gently lifted and clamped at the aorta using a haemostat. The hearts were subsequently cut away from the thoracic cavity and mounted onto a 3D-printed platform, such that the apex of each heart was facing up-ward.[15,89] Hearts were then perfused with *EDTA buffer* at 6mL/min for ~5 minutes. Once hearts had sufficiently cleared with any residual blood, the perfusion rate was reduced to 4mL/min and the perfusate was changed to a collagenase and protease *digestion buffer*,[90] for ~15 minutes. All buffers were maintained at 37°C throughout the perfusion process.

Hearts were then further dissociated by gently separating the tissue with forceps before incubating the cell suspension for a further 10-minutes, at 37°C. Cardiac non-myocytes were separated from cardiomyocytes and other cellular debris and subject to antibody/viability-dye staining. Stained non-myocytes consequently underwent fluorescence-activated cell sorting (FACS, BD FACS Aria™ Fusion Flow Cytometer, Alfred Research Alliance Flowcore) as described previously.[14,15] Live (SYTOX™ Green$^-$), metabolically active (Vybrant™ DyeCycle™ Ruby$^+$) cardiac non-myocyte cells were sorted into endothelial cells (CD31$^+$), leukocytes (CD45$^+$), and resident mesenchymal cells (CD31$^-$CD45$^-$).

Major non-myocyte cell populations were manually counted using a haemocytometer, after which samples were pooled based on their genotype (*db/h* or *db/db*). Each pooled sample consisted of ~12,000 cells (ECs; ~10%, RMCs; ~90%) when loaded into the 10X Chromium controller for single cell library preparation (Chromium Single Cell 3' v2, lane 1: pooled *db/db* non-myocytes [*n=4*], lane 2: pooled *db/h* non-myocytes [*n=3*]). Individual cells were captured and lysed within the 10X controller, after which cDNA was synthesised and amplified for a total of 12 cycles. Amplified cDNA was then sequenced. Sequencing was performed on an Illumina NovaSeq 6000 system to an approximate depth of 100,000 reads per cell.

QUANTIFICATION AND STATISTICAL ANALYSIS

In silico analysis of scRNAseq data

Raw sequencing data files were processed using Cell Ranger software version 5.0.0 (10X Genomics) prior to subsequent analysis. This pipeline aligned the sequencing reads from fastq files to the reference genome *Mus musculus* (mm10) and quantified the expression of transcripts within each cell. Then, the analyses of these processed scRNA-seq data were carried out in R studio version 4.1 using Seurat suite version 3.2.0. Pre-processing of scRNAseq data was conducted as previously described.[15] This yielded a total of 9,316 cardiac non-myocyte cells. Clustering of cells was primarily depicted via t-distributed stochastic neighbour embedding (tSNE) projection, which reduces highly complex data to two dimensions for interpretation. Cell types were annotated by querying established cell marker genes as described previously[15] and by considering the top-5 most highly-expressed genes in each cell cluster.

Differential gene expression analysis

Differential expression (DE) analysis was performed to identify DE genes between groups per cell type. Genes that have non-zero expression in >10% of cells in at least one of the experimental groups were considered in this analysis. The DE testing method 'MASTcpmDetRate' was used to identify DE genes between groups. This test is a modification of 'MAST',[91] considering cellular detection rate as a covariate, which has been successfully performed in a benchmark study for detecting differential expression from scRNA-seq.[92] To determine statistical significance of DE genes between experimental groups, the uncorrected *P* value threshold was set at < 0.01, unless otherwise stated.

Gene ontology analysis

Gene Ontology (GO) enrichment analysis was performed using the 'enrichGO' function within the 'clusterProfiler' R package version 3.12.0.[93] All GO analyses presented were mapped to reference genomes retrieved from http://geneontology.org. Enrichment analysis of GO Biological Process terms (GO-BP) was calculated by mapping our list of differentially expressed genes (uncorrected *P* value < 0.01) to the default background gene list for *Mus musculus*, with minimum and maximum gene set sizes 10 and 500, respectively. Systematic similarities between GO terms were calculated using the 'simplify' function within the clusterProfiler R package. The GO-BP terms that had semantic similarity higher than the specific cut-off point of 0.7 were considered as redundant GO-BP terms and thus discarded from analysis. The Benjamini-Hochberg adjusted *P* value cut-off of 0.05 was used to determine statistically significant GO-BP terms. More specific information was derived based on statistically significant GO terms identified in our analysis.

Ligand-receptor intercellular communication analysis

Intercellular communication between cardiac non-myocytes was inferred in silico, using CellPhoneDB version 2.1.7, which utilises various repositories relating to cellular communication by considering the subunit architecture of both ligands and receptor genes (Efremova et al., 2020). To investigate cell-cell communication network using CellPhoneDB, a cell type annotation file and a normalised gene count matrix

were extracted from the annotated Seurat object. The total number of communication signals transmitted and received by a certain cell population was quantified and visualised in a heatmap.

To further explore specific ligand-receptor signalling networks between cardiac cell populations, mouse orthologs of human ligand-receptor pairs (Ramilowski et al., 2015) were obtained from BioMart database v100 using the biomaRt R package. Ligand/receptor genes with non-zero expression in over 20% of cells in a particular cell population were considered "expressed". These expressed ligands were then connected to their corresponding receptors within and between the major cell populations to construct a potential cell-to-cell communication network. The signalling direction from ligand to receptor is indicated by arrows in the chord plots, and the total number of communication signals transmitted and received by a certain cell population is represented by the numbered bands in the circular visualization. The Circlize R package was used to create circular visualizations.

In addition, GO analysis was also performed on both ligands and receptor in *db/db* hearts relative to *db/h* controls to determine their biological relevance. The total number of communication signals transmitted and received by a certain cell population was also quantified.

Incorporation of bulk RNA-sequencing data

To validate our cardiac non-myocyte scRNAseq findings, we incorporated differentially expressed genes acquired from two additional, publically available bulk RNA sequencing (bulk RNA-seq) datasets[42,43] into our gene list and developed a proportional Venn diagram using R packages, RVenn (v1.10), Euller (v6.10), VennDiagram (v1.6.20) and Venneuler (v1.1-0). Differentially expressed genes from all datasets were filtered by *P* value ($P < 0.01$ for bulk RNA-seq, $P < 0.001$ for scRNAseq data). Common differentially expressed genes were identified using the 'overlap' function within RVenn. Differentially expressed gene lists were obtained and data was visualised using Venneuler R package. The hypergeometric p values for overlapping gene sets were calculated using 'phyper' function in stats R package considering all genes identified in the scRNA-seq dataset as the total number of genes. Subsequently, GO analysis was performed on each overlapping gene list derived from this analysis to produce biologically relevant pathways specific to each set of overlapping genes.